PERFORMANCE AND FLOW DYNAMICS IN CROSS-FLOW TURBINES

Miguel Somoano Rodríguez

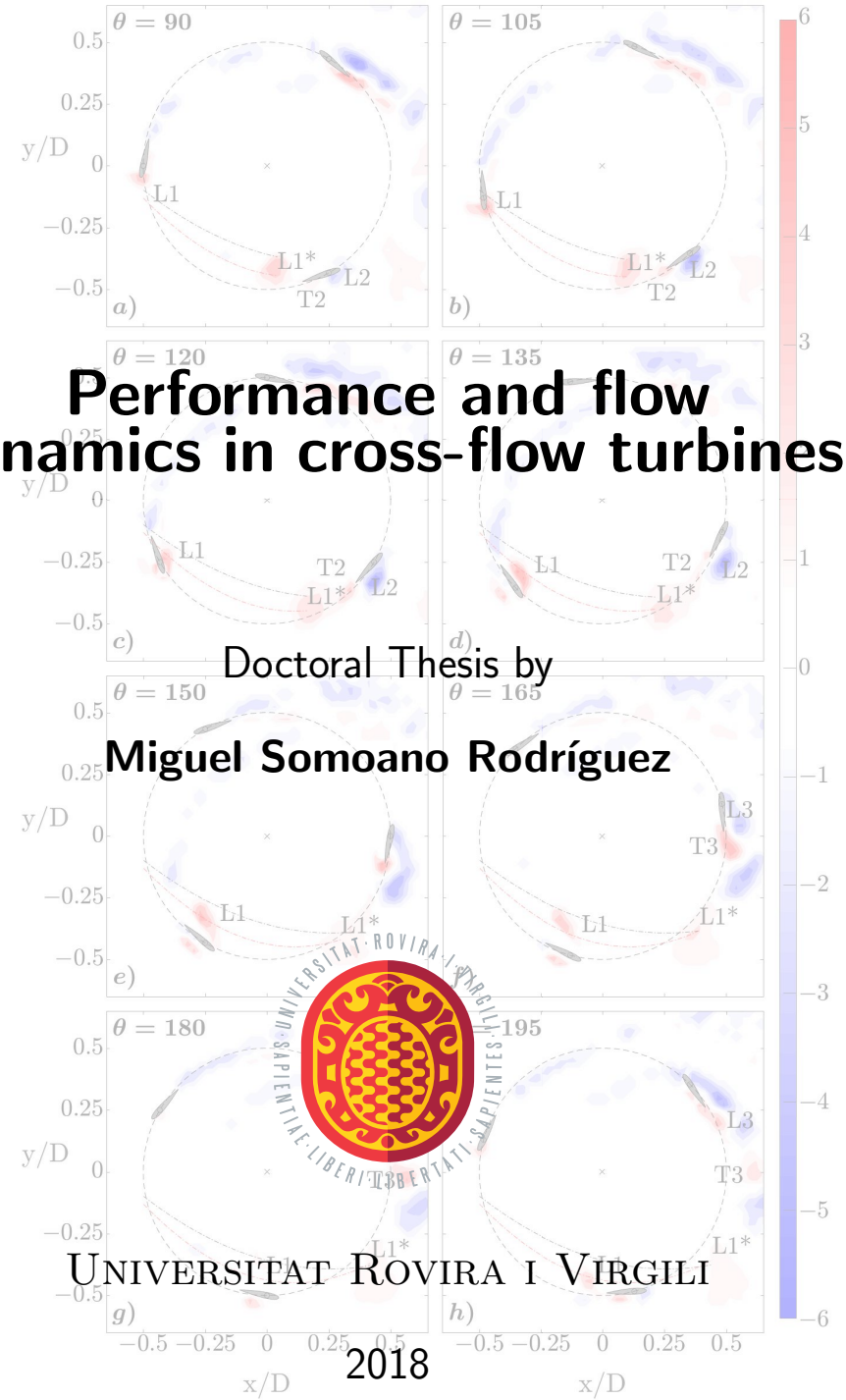

Performance and flow dynamics in cross-flow turbines

Doctoral Thesis by

Miguel Somoano Rodríguez

Universitat Rovira i Virgili

2018

UNIVERSITAT ROVIRA I VIRGILI
PERFORMANCE AND FLOW DYNAMICS IN CROSS-FLOW TURBINES
Miguel Somoano Rodríguez

UNIVERSITAT ROVIRA I VIRGILI
PERFORMANCE AND FLOW DYNAMICS IN CROSS-FLOW TURBINES
Miguel Somoano Rodríguez

UNIVERSITAT ROVIRA I VIRGILI
PERFORMANCE AND FLOW DYNAMICS IN CROSS-FLOW TURBINES
Miguel Somoano Rodríguez

Performance and flow dynamics in cross-flow turbines

Doctoral Thesis by

Miguel Somoano Rodríguez

supervised by Dr. Francisco J. Huera Huarte

Department of Mechanical Engineering

Universitat Rovira i Virgili

Tarragona 2018

UNIVERSITAT ROVIRA I VIRGILI
PERFORMANCE AND FLOW DYNAMICS IN CROSS-FLOW TURBINES
Miguel Somoano Rodríguez

UNIVERSITAT ROVIRA i VIRGILI

DEPARTAMENT D'ENGINYERIA MECÀNICA

Escola Tècnica Superior d'Enginyeria Química
Av. dels Països Catalans, 26
43007 Tarragona (Spain)
Tel. +34 977 55 96 02 secmec@urv.cat
Fax +34 977 55 96 93 www.etseq.urv.es/DEM/

I STATE that the present study, entitled "Performance and flow dynamics in cross-flow turbines", presented by Miguel Somoano Rodríguez for the award of the degree of Doctor with International Mention, has been carried out under my supervision at the Department of Mechanical Engineering of this university.

Tarragona, 20 de abril de 2018

Doctoral Thesis Supervisor

CPISR-1 C Francisco Javier Huera Huarte

Firmado digitalmente por CPISR-1 C Francisco Javier Huera Huarte
Nombre de reconocimiento (DN): c=ES, o=Universitat Rovira i Virgili, ou=Vegeu https://www.aoc.cat/CATCert/Regulacio, sn=Huera Huarte, givenName=Francisco Javier, serialNumber=39888633D, cn=CPISR-1 C Francisco Javier Huera Huarte
Fecha: 2018.04.20 12:34:49 +02'00'

Dr. Francisco J. Huera Huarte

Acknowledgements

Firstly, funding provided by the Spanish Ministerio de Economía y Competitividad through grants BES-2013-065366 (for doctoral formation at Universitat Rovira i Virgili) and EEBB-I-16-10931 (for a short stay at University of Washington) is gratefully acknowledged.

Secondly, I would like to thank Prof. Miguel Losada for transmitting me the passion for science, and Dr. Alberto Aliseda for his valuable teachings. I feel especially lucky of having shared this long and winding road with Dr. Francisco Huera, who has been like an older brother showing me the wonderful world of the experimental research.

Finally, I am very thankful to all my family: to my grandparents, Chus and Mª Arís for sharing their wisdom, humility and patience; to Julio for encouraging me to fight for what I want; to Yago for making me love engineering; to my father for teaching me that effort always has a reward; and to my mother for believing always on me (even more than myself). I am especially grateful to Lucía for her love and continuous support: no matter how dark the tunnel was, her light always illuminated its end.

"Science is like sex: sometimes something useful comes out, but that is not the reason we are doing it." – Richard P. Feynman

Abstract

This doctoral thesis presents the study that the author have carried out in order to understand the effect of the blade pitch angle on the blade-wake interactions that take place inside the rotor, and hence on the performance of a three straight bladed Cross-Flow Turbine (CFT).

Firstly, we have experimentally studied the performance of this kind of turbine with its blades based on a NACA-0015 profile and a chord-to-diameter ratio $c/D = 0.16$ at a Boundary Layer Wind Tunnel (BLWT) facility. We have done it with nine different fixed blade pitches between $\beta = 8°$ toe-in and $\beta = 16°$ toe-out, at three different turbine diameter Reynolds numbers covering the transitional region $3 \cdot 10^5 < Re_D < 5 \cdot 10^5$ in which the torque produced by the blades overtakes the opposed resistive torque. Due to the air bearings, the resistive torque has been high conditioned by the aerodynamic drag. Although we have used a DC motor to surpass the lack of self-starting, we have taken all the measurements without the forcing imposed.

Shape and values of the performance curve change drastically with just an increment of 2° in the fixed pitch angle, obtaining the best performance inside the range $4^\circ < \beta < 8^\circ$ toe-out. Moreover, depending on the Re_D, the ideal β and the optimal Tip Speed Ratio (TSR) at which the maximum dimensionless power output of the turbine takes place vary. The higher the Re_D, the lower the optimal tip speed ratio and the more towards toe-out the ideal pitch angle is.

Afterwards, we have experimentally studied the flow dynamics inside the rotor of a CFT of smaller scale but with the same characteristics of solidity and blade profiles, for different blade pitches. The turbine model has been designed in order to quantify the flow inside and around the rotor using planar Digital Particle Image Velocimetry (DPIV). Tests have been made by forcing the rotation of the turbine with a DC motor, which has provided precise control of the tip speed ratio, while being towed in a still-water tank at a constant turbine diameter Reynolds number of $6.1 \cdot 10^4$. The range of TSRs covered in the experiments has gone from 0.7 to 2.3. The focus has been given to the analysis of the blade-wake interactions inside the rotor.

Toe-in and excessive toe-out angles have been associated to low performances of this type of turbines, that is why three pitch angle cases β of 8° toe-in, 0°, 8° and 16° toe-out have been chosen, with the aim to study in detail the blade-wake interactions inside the rotor. The investigation has allowed us to relate the blade-wake interactions with the

turbine performance differences, as a function of both the operational tip speed ratio and the blade pitch angle.

Contents

Chapter 1

Literature review

1.1 Antecedents

The Cross-Flow Turbine (CFT), usually designated as Vertical Axis Wind Turbine (VAWT), which first version was designed by the French aerospace engineer Georges J.M. Darrieus [16], is characterized by having its shaft cross to incoming flow and being induced by lift forces. This type of VAWT is preferred to the drag-type one developed previously by the Finnish architect Sigurd J. Savonius [46] because, despite its lack of self-starting [18], Darrieus rotor has a higher efficiency [27] being designed for Tip Speed Ratios (TSRs) greater than one [40]. The tip speed ratio is defined as the ratio between the tangential speed of the

blade due to its rotation and the free stream velocity

$$\lambda = \frac{\omega D}{2u_\infty} \tag{1.1}$$

with D being the rotor diameter, ω the angular velocity of the rotor, and u_∞ the free stream velocity. The CFTs can be used to transform either wind or tidal energy.

Both wind and tidal power are renewable energies, i.e. they are obtained from virtually inexhaustible natural sources, either by the immense amount of energy that they contain or because they are able to regenerate by natural means. The final boost to use wind as an energy source has its origin in the 1973 oil crisis. While replacing fossil fuels with nuclear energy quickly found its detractors, interest grew in renewable ones with current and future availability guaranteed. Thus, in order to exploit the resources of the earth ecologically, new competitors to the already established hydro power were begun to look for.

As initially these energy sources were not profitable, international governments promoted the change in energy policy in the form of subsidies and research programs. In 1979, with the second oil price increase, the Spanish Ministry of Industry and Energy launched the first research and development program aimed at harnessing wind energy for producing electricity. Nowadays, this clean and renewable energy source covers more than 20% of electricity demand in Spain. In fact, Spain is the

fourth largest producer of wind power in the world, with $23\,GW$ of installed capacity, just behind China, USA and Germany. In 2011, the Spanish Government approved in its National Plan for Renewable Energies for 2020 wind targets of $35\,GW$ of installed power capacity onshore, and $3\,GW$ offshore.

While nowadays wind energy already covers more demand than hydro power in Spain, not a single tidal power plant has been projected yet. Whatever the origin of the stream, the main idea is to extract kinetic energy of the flow available. Although investment to build these plants that harness tides as a source of clean and renewable source is certainly high, the fact remains that for the same flow rate, tidal power is ten times greater than wind power.

1.2 Cross-flow turbines vs axial-flow turbines

The largest wind farms and tidal power plants use Axial-Flow Turbines (AFTs), also referred to as Horizontal Axis Wind Turbines (HAWTs), obtaining an efficiency on the primary process even higher than 0.5 [52]. These rotors with their shaft oriented as the incoming flow are also induced by lift forces, which in this case may be preferred to drag-type for developing less intense wakes apart from other aerodynamic considerations [35]. However, in the last decade there has been an increased

interest for Cross-Flow Turbines and their capabilities for energy harvesting, whatever the origin of the stream is [10, 53].

The cheapest manufactured version of CFTs is the Giromill turbine or H-rotor, defined by their straight blades with constant cross-section profiles. Its geometry has some advantages over curved-blades on the aerodynamic performance, but that is penalized by large bending moments resulting in lower efficiency. Nevertheless, in the case of small straight-bladed Darrieus rotors, the effect of the gravitational field is negligible when compared to the centrifugal force field produced by the rotation of the blade in full operation [40].

Ideally we desire systems that be the most easily adjustable with respect to the current and scalable. Straight-bladed CFTs, despite having bad starting characteristics, have several advantages in comparison to AFTs: omni-directionality, lower manufacturing and maintenance costs, less noise emittance, and better mechanical performance in unsteady and skewed wind conditions with complex flow patterns such as high wind velocities and turbulent wind flows [3, 15, 26, 29, 36, 39]. Furthermore, efficiency on ideal Darrieus rotors can be in theory as high as 0.72 [25], well over the limit of $16/27 = 0.5926$ imposed by Betz's law [9]. However, the performance of CFTs is far from this unreachable value, fact that could be in part attributed to a lack of understanding of the complex flow phenomena inside the rotor.

The actual performance of VAWTs causes this kind of turbines not to be so economically attractive and to be just installed isolated in areas where HAWTs are not worthy, like in the mountains or in urban environments. This way, the ability of CFTs to work as a whole in farms, causing a greater efficiency per unit area or volume when considering interactions between adjacent counter-rotating machines, is rendered useless. Dabiri [14], and Whittlesey et al. [54] claimed that the overall performance of the CFT farms could be considerably superior to the AFT farms in terms of power generation per ground area.

1.3 Performance curve

The performance curve results from plotting the power coefficient as a function of TSR, and are widely used to represent the efficiency of turbines. The power coefficient is the dimensionless form of the power output, defined as

$$C_P = \frac{2T\omega}{\rho L D u_\infty^3} \tag{1.2}$$

where T is the net torque applied on the shaft, ρ is the fluid density, and L the blade span. Kjellin et al. [30] performed a measurement campaign on a three straight bladed CFT in order to obtain its $C_P(\lambda)$ curve. The rotational speed of the generator used was controlled in order to keep

the turbine velocity constant, while the wind speed was systematically changed at the facility.

An important parameter with great influence on the turbine performance is the Reynolds number based on the turbine diameter

$$Re_D = \frac{u_\infty D}{\nu} \tag{1.3}$$

where ν is the fluid kinematic viscosity, being the dimensionless number the ratio of inertial forces to viscous forces acting on a fluid. In order to obtain the performance curve of a three straight bladed CFT, Bachant and Wosnik [4] towed their model in a water tank. The turbine had blades with NACA-0020 profile, and a chord-to-diameter ratio (c/D) of 0.14. Their experiments were all conducted at the same speed, with a constant Re_D of $1.0 \cdot 10^6$. Tip speed ratio was prescribed and held constant during each run, by using a servo motor coupled to the turbine shaft. Their experiments showed a maximum power coefficient of 0.26 at a tip speed ratio of 1.9. By changing Re_D in the range from $3.0 \cdot 10^5$ to $1.3 \cdot 10^6$ [6], they observed a drastic improvement in the dimensionless power output of the CFT.

Bravo et al. [11] used a three straight bladed CFT model with NACA-0015 blades and a c/D ratio of 0.16 to carry out experiments in a full-scale wind tunnel for a range of diameter Reynolds number from $1.0 \cdot 10^6$ to $2.7 \cdot 10^6$. They measured the torque with a load cell, and used an

active closed-loop speed control system which accurately regulated the rotational velocity of the rotor. They controlled the speed because the system was not self-regulating at the lowest TSRs of the performance curve, before reaching the maximum power output. With a constant load, the CFT was not able to keep its angular rotating speed ω, it tended either to slow down until stopping or to head to higher speeds. At all Re_D investigated the maximum power coefficient occurred at a tip speed ratio $\lambda \approx 1.6$, and for $Re_D \geq 1.3 \cdot 10^6$ the performance curve became essentially Re-independent. Remarkably, they did not obtained the maximum C_P, close to 0.3, at the highest Reynolds number, but at a $Re_D = 1.7 \cdot 10^6$. Fiedler and Tullis [22] conducted identical experiments but at lower turbine diameter Reynolds numbers, $8.3 \cdot 10^5 < Re_D < 1.8 \cdot 10^6$, showing consistent results.

In the work by Takao et al. [50], the authors used a three straight bladed CFT, but this time based on asymmetric NACA-4518 profiles, with a c/D ratio of 0.17. The experiments were performed in a open-jet wind facility at $Re_D = 3.2 \cdot 10^5$, and a maximum power coefficient $C_P = 0.11$ was obtained at a tip speed ratio $\lambda = 1.7$. Li et al. [32] investigated a four straight bladed CFT with a chord-to-diameter ratio $c/D = 0.13$ and NACA-0021 blades. In addition to a torque meter, the authors used a six-component balance to measure the loads on the turbine at a $Re_D = 1.1 \cdot 10^6$. The power coefficient slowly rises up to $C_P \approx 0.15$ and then from $\lambda = 1.7$ rapidly decreases. Figure 1.1 compiles some of the performance curves obtained experimentally by all

these authors, with turbine solidities

$$\sigma = \frac{Nc}{\pi D} \tag{1.4}$$

in the range from 0.13 to 0.17, for comparison.

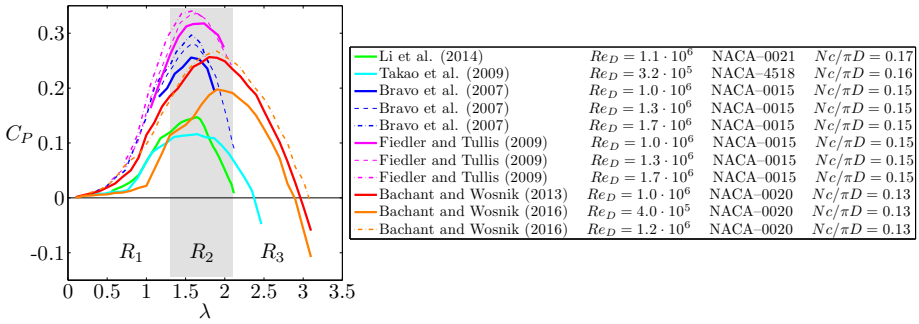

Figure 1.1: Dimensionless performance curves associated to different studies with turbines of similar solidity in works reported by some authors, at several Re_D.

As it can be seen in the figure, the shape of performance curves of cross-flow turbines show three clearly distinct and well defined regions as a function of the tip speed ratio. In the first region (R1), for the lowest TSRs, the power coefficient grows monotonically. For intermediate TSRs, in the second region (R2), the C_P exhibits its maximum values. In the third region (R3), for the highest TSRs, the C_P drops abruptly. In Figure 1.1, the second region or R_2, in which the performance is higher, appears shaded for reference. The intention here is not to define these three regions in a closed manner, i.e. describing the λ at which each region starts and ends, but to emphasize from a qualitative perspective, how for sufficiently low or high λ, the performance of this type of tur-

bines is considerably lower than that typical in the second region. It is also well known that decreasing the turbine solidity yields increases in the value of λ that maximizes the performance of the turbine [12, 34, 43]. Moreover in Figure 1.1, by varying the velocity of the incoming flow, and hence the Re_D, the value of the maximum power coefficient is modified but the ranges of TSRs at which these three different regions take place, remain practically the same.

1.4 Wake

Rolin and Porté-Agel [44] used 2D-3C stereo Digital Particle Image Velocimetry (DPIV) in a closed-looped Boundary Layer Wind Tunnel (BLWT) to study the wake behind a three straight bladed CFT at a turbine diameter Reynolds number $Re_D = 4.1 \cdot 10^4$ and a tip speed ratio $\lambda = 2$. They distinguished two important regions of the wake: one behind the blades of the rotor as they move upwind, and the other as they move downwind. These two regions will be termed from now on the upstroke and the downstroke region, respectively. The azimuthal angle θ is defined in Figure 1.2, taking the counter-clockwise direction as positive. In the figure, the flow is left to right, hence the upstroke region covers the range $-90° < \theta < 90°$ and the downstroke region, $90° < \theta < 270°$. In Rolin and Porté-Agel [44], the upstroke region of the wake was associated with a significantly larger velocity deficit and a

higher level of turbulence than the downstroke part. The upstroke side of the wake also tended to expand and diffuse into the unperturbed flow to a greater extent than the downstroke one. This was primarily the result of the higher levels of turbulence produced by large wind shear in the upstroke region, but might be due in part to the crosswind momentum imparted on the flow by the rotation of the turbine. In the core of the wake, momentum was transferred from the downstroke side of the wake to the upstroke one, such that far downstream the wake became more symmetric. In Figure 1.2, the upstream region covers the range $0° < \theta < 180°$ and the downstream region, $180° < \theta < 360°$.

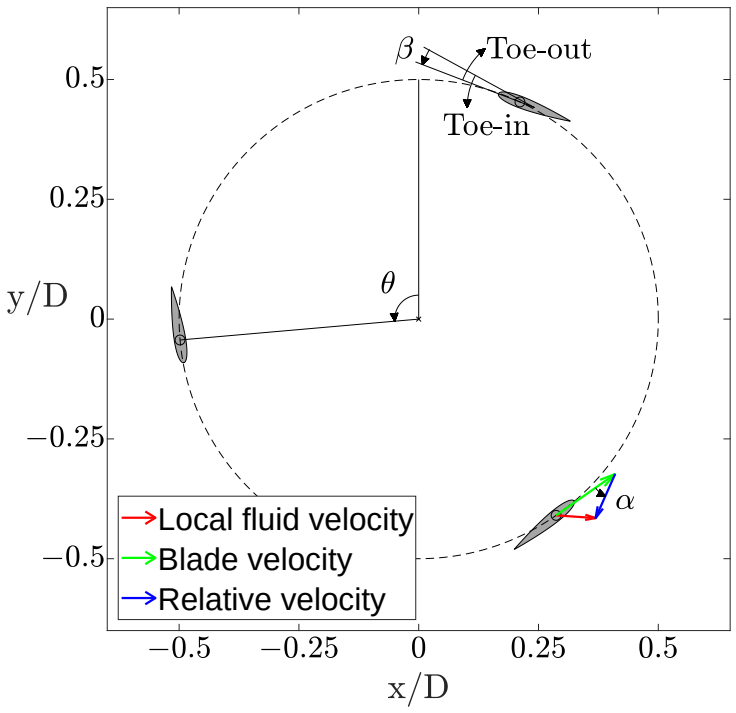

Figure 1.2: Schematic cross-sectional view of a CFT rotor.

According to Barsky et al. [8], as the stall phenomena declines, the wake is wider. Dynamic stall in an airfoil takes place during the rapid transient motions in which the effective angle of attack surpasses the static stall limit (as detailed in Section 1.5). Tescione et al. [51] decided to use 2D-2C and 2D-3C DPIV techniques in a closed-circuit open-jet wind tunnel to observe the wake of a two straight bladed CFT for a $Re_D = 6.2 \cdot 10^5$, at a TSR of $\lambda = 4.5$ in order to avoid dynamic stall. In the near wake $x/D < 1.5$ (being x here the distance in the flow direction, downstream the turbine shaft), they showed the cycloidal pattern of vorticity as a result of a wake released by a blade which was moving in a circular motion and transported downstream, with the vortex tubes released by the blades tips retaining the similar cycloidal shape. In the far wake $x/D > 1.5$, at the upstroke and downstroke edges of the rotor area, the passage of the blade through previously released wakes caused the blades wakes were no longer detectable, and the vortices at the edges of the wake were the only dominant structures.

Bachant and Wosnik [5] showed that near wake statistics such as mean velocity, turbulence intensity and Reynolds shear stress, varied very weakly over the range of Re_D from $3 \cdot 10^5$ to $1.3 \cdot 10^6$. In the work by Parker and Leftwich [41], the authors reported that the general structure of the time-averaged stream-wise velocity in the wake was very similar over a wide range of Re_D (from $6{\cdot}10^4$ to $1.8{\cdot}10^5$). The turbine they used was a three straight bladed model with a c/D ratio of 0.16. These authors conducted their experiments with a model

that was not flow-driven, but motor-driven because of the low Re_D at which the facility was limited, arguing that the dynamics in the wake were the same in both situations. The aim was to study and compare the results obtained in the laboratory with a motor-driven turbine, to those of a flow-driven full scale machine that operated at considerably higher Re_D. The comparison between a flow- and a motor-driven turbine was in fact first investigated by Araya and Dabiri [2], who found a very weak dependence of the wake mean velocities on Reynolds number, but a very strong dependence on TSR over the range of Re_D from 3.7·10^4 to 7.8·10^4. The authors reported measurements in the near wake of their turbine, for comparison between a flow-driven and a motor-driven CFT model, using DPIV. They found nearly identical stream-wise and lateral mean velocity profiles, lateral velocity fluctuation power spectra, shaft torque, and circulation in the wake in both situations, flow-driven and motor-driven, over a TSR range of $1.2 < \lambda < 1.7$. They concluded that the kinematics of the spinning turbine, not the method by which it is set in motion, determines the wake dynamics. Based on their assumption it appears obvious that a motor-driven turbine can be used in order to study the flow dynamics and the blade interactions in turbines, even if Re_D typical of flow-driven machines are not achieved.

1.5 Angle of attack

The blades of a CFT see a periodically changing incoming flow during their rotation, with large variations of lift and very complex stall phenomena taking place depending on their velocity relative to the local flow. In Figure 1.2, the angle of attack α is presented as the angle formed by the blade velocity and the flow velocity relative to the moving blade vectors. Both vectors and the absolute flow velocity formed the velocity triangle in the vicinity of the blades [45]. The fluid velocity relative to the moving blade is found as the difference of the other two velocity vectors. The sign convention of taking the counter-clockwise direction as positive for the rotor azimuthal angle θ, is also used for the blade angle of attack α, i.e. positive when the relative velocity passes across the blade travelling outward from the centre of the turbine. Assuming the airfoil has negligible influence on the flow field, and hence neglecting induced velocities, α only depends on the TSR and the azimuthal angle according to the analytical expression [28, 40]

$$\alpha = -\tan^{-1}\left(\frac{\sin\theta}{\lambda + \cos\theta}\right) \tag{1.5}$$

Sheldahl and Klimas [47] showed a static stall angle of $\alpha_{ss} \approx 14^{\circ}$ with a NACA-0015 airfoil experimentally tested at a wind tunnel for a range of turbine diameter Reynolds number of $3.6 \cdot 10^5 < Re_D < 6.8 \cdot 10^5$. For the same symmetric airfoil, Morshed et al. [38] described a similar

value of the static stall angle, preceded by a sudden increase of drag force coefficient at $\alpha = 12°$ for a range of Re_D from $1.4 \cdot 10^5$ to $3.8 \cdot 10^5$. Numerically Rezaeiha et al. [42] using CFD at $Re = 1.2 \cdot 10^5$, and experimentally Gerontakos and Lee [24] at $Re = 8.7 \cdot 10^4$, obtained an $\alpha_{ss} \approx 13°$ with the NACA-0015 profile. The dynamic stall angle will be even higher than the static value. The boundary layer on the suction side of the rotating airfoil remains attached and the lift force increases with angle of attack beyond the static stall angle. The increase in the drag force experienced by the airfoil is delayed and becomes more abrupt than the lift force one. When the flow separates the shear layer rolls-up to form a Leading-Edge Vortex (LEV). At some point, the benefit due to the increase in lift force on the airfoil starts to be smaller than the negative effect due to the increase in drag force [37, 13].

1.6 Angle of pitch

In Figure 1.2, the blade pitch β is defined as the angle between the foil centreline and the line tangent to the circular trajectory of the blade, at its mid-chord. A forward shift of mount-point from the centre of the chord towards the leading edge, corresponds to an effective toe-in pitch change of

$$\beta = \tan^{-1}\left(\frac{2x}{D}\right) \tag{1.6}$$

where x here is the distance between these two points along the blade chord [22].

If induced velocities are neglected, but $\beta \neq 0°$, the angle of attack also depends on the blade pitch angle. Kirke [28] expressed analytically this relation as

$$\alpha = -\tan^{-1}\left(\frac{\sin\theta}{\lambda + \cos\theta}\right) + \beta \tag{1.7}$$

where β is positive in the toe-in rotation. Therefore, the blade pitch angle is another parameter with huge influence on efficiency of cross-flow turbines. Fiedler and Tullis [22] studied how the performance curve varied as a function of the preset fixed pitch on the blades. With a $\lambda = 1.6$, the authors obtained a better performance as they were moving from $\beta = 6.4°$ toe-in to $\beta = 5.3°$ toe-out, passing through $\beta = 2.5°$ toe-in and $\beta = 1.4°$ toe-out. Li et al. [33] repeated the experiment of Li et al. [32] on a two straight bladed CFT model with a c/D ratio of 0.13, changing the pitch angle in $2°$ steps from $\beta = 4°$ toe-out to $\beta = 8°$ toe-out. The turbine performance increased up to $C_P = 0.21$ at $\lambda = 2.2$ when adjusting the blade pitch from $\beta = 4°$ to $\beta = 6°$ toe-out, but decreased when moving β from this last value to $8°$ toe-out.

El-Samanoudy et al. [20] with their four straight bladed CFT based on NACA-0024 airfoil with a chord-to-diameter ratio $c/D = 0.19$ in a wind open-jet facility at a $Re_D = 4.3 \cdot 10^5$, also observed that the maximum

dimensionless power output began to decrease at some value of toe-out pitch. Using load cells to measure the tension of a rope in contact with a grooved pulley attached to the shaft, they found a maximum power coefficient of 0.25 at $\lambda = 1.3$ for a β of $10°$ toe-out. The maximum C_P for both $\beta = 0°$ and $\beta = 20°$ toe-out, were smaller and took place at lower TSR. Strom et al. [49] tested straight bladed CFTs with two and four NACA-0018 blades with a c/D ratio of 0.24 in a water flume facility at $Re_D = 1.2 \cdot 10^5$, covering the range of pitch angles $0° < \beta < 12°$ toe-out with increments of $2°$. They operated a servo motor in constant velocity mode via the shaft to measure the turbine torques with a six-axis load cell. Obtaining the maximum $C_P = 0.18$ for the two-bladed CFT, in both cases the best scenario took place with $\beta = 6°$. Logically the optimal tip speed ratio $\lambda = 1.8$ for the two-bladed CFT was higher (as its solidity was lower), but in both cases the performance curve had two clearly defined peaks. If in this part of the curve between the two peaks, the net blade torque is negative, i.e. the resistive torque is superior to the aerodynamic torque of the blades, this region is called *dead band* [7], and it is typical of CFT models on a small scale.

Chapter 2

Aims

2.1 Main objective

The purpose of this Doctoral Thesis is to understand the effect of blade pitch on the performance and flow dynamics inside cross-flow turbines. However, for this purpose it is necessary to first study the dependence of rotor behaviour on other inseparable variables such as the turbine diameter Reynolds number and the tip speed ratio. In order not to complicate more the analysis, we maintain constant the number of blades and the chord-to-diameter ratio, i.e. the turbine solidity, and the symmetric profile of the blades in all the experiments we carry out.

2.2 Specific goals

To reach the main objective, we set the following specific targets, namely:

1. Design and manufacture of a three straight-bladed cross-flow turbine that can be tested inside the boundary layer wind tunnel facility located in the Laboratory for Fluid-Structure Interaction (LIFE) at Universitat Rovira i Virgili (URV), in order to obtain performance curves. The model must achieve high Reynolds numbers with the velocity limitations of the wind tunnel, avoiding blockage effects due to the test-section dimensions. Besides, the resistive torque of the system should allow the turbine to reach high tip speed ratios.

2. Obtaining measurements of the performance of the model for uniform flows at different free stream velocities, that allow us to understand the dead band phenomenon and its dependence on the blade pitch angle.

3. Design and manufacture of a three straight-bladed CFT to be tested inside the water tank facility also located in the LIFE at URV, in order to carry out DPIV measurements. The model must reach tip speed ratios and Reynolds numbers as high as possible with the velocity limitations of the facility, avoiding blockage effects. Besides, it should allow the camera to record inside the rotor and the near wake downstream.

4. Carrying out optical measurements of the velocity field for a uniform flow at different rotational speeds. The possibility of quantifying the flow, and its relation to the efficiency of the machine for different pitch configurations, is crucial to understand the physics of the problem.

5. Discussion and analysis of the results, and proposal of better alternatives for future designs.

Chapter 3

Performance of cross-flow turbines

3.1 Introduction

Edwards et al. [19] tested a three straight bladed CFT in a wind tunnel with an open section at a $Re_D = 3.1 \cdot 10^5$. They used a motor which could be engaged/disengaged via an electromagnetic clutch, to drive the turbine up to high speeds through the dead band. Once the motor was disengaged, a brake torque was applied by a hysteresis brake. Araya and Dabiri [2] defined the rotor *neutral curve* as the $\lambda(Re_D)$

curve that shows the upper bound of tip speed ratios for flow-driven cases, i.e. the maximum λ values that the rotor reaches if flow-driven. Their empirical curve was shifted lower because of the inherent losses of the turbine system, and was monotonically increasing except from around $Re_D \approx 6 \cdot 10^4$ where there was an abrupt rising. Moreover they obtained good agreement between the torque measurements of motor-driven and flow-driven cases using a rotary torque sensor at a diameter Reynolds number $Re_D = 7.8 \cdot 10^4$, when operating on the back side of the performance curve (after reaching the maximum power output) where the CFT can operate in steady state.

The objective of this chapter is to describe the effect of Reynolds number and blade pitch on the performance of a cross-flow turbine. For this purpose, we will obtain different performance curves in a range of Re_D that covers the transitional region in which the aerodynamic torque of the blades overtakes the resistive torque, and analyse how small variations of β modify the shape of these curves, hence the behaviour of this turbine.

3.2 Experimental set-up

The experiments were carried out in the BLWT of the Laboratory for Fluid-Structure Interaction, at Universitat Rovira i Virgili in Tarrag-

ona. The facility is an open-circuit blower tunnel with an axial fan that forces the air into the settling chamber through a diffuser. The settling chamber is composed of an array of three honeycombs to reduce turbulence intensity and supply a more uniform flow to the contraction section which accelerates the flow. Wind speeds up to $12\,m/s$ can be reached. The wind tunnel has a total length of $23\,m$ and a working section of $1.84 \times 1.22\,m^2$ with $14\,m$ of optical access. As Figure 3.1 shows, the model was placed at the beginning of this test-section (where the boundary layer is not developed) and centred (to avoid wall effects), in order to have a uniform flow with low turbulence intensity.

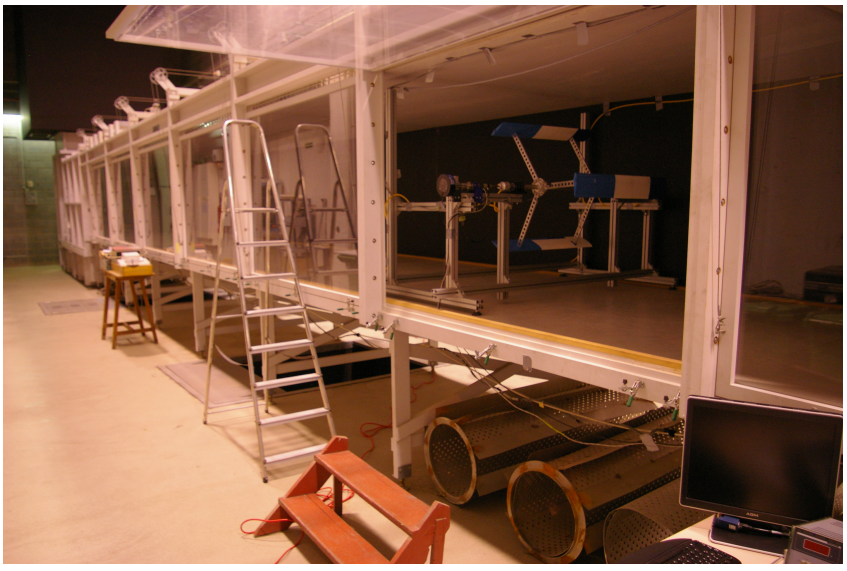

Figure 3.1: Cross-flow turbine inside the test-section of the boundary layer wind tunnel.

Our turbine model consisted on a three straight bladed cross-flow turbine with its blades based on NACA-0015 airfoil and printed in Poly-

Lactic Acid (PLA). The blades had a chord of $0.12\,m$ and a total span of $0.75\,m$ with an inner core made of an aluminium square tube of $8\,mm$ side, that provided very high flexural stiffness to the blades. The blades were connected to a horizontal stainless steel shaft of $25\,mm$ diameter through six aluminium struts located at $1/5$ and $4/5$ of the blade spans. The turbine diameter was $D = 0.75\,m$ leading to a chord-to-diameter ratio of $c/D = 0.16$, and a span-to-diameter ratio of $L/D = 1$. Connections between the aluminium squared tube that acted as the core of the blades and the two struts were also printed in PLA and allowed the blades to be oriented with the desired fixed pitch angle. Experiments were conducted with 9 different β, taking into account the effective toe-in pitch change of Equation 1.6 for a forward shift of mount-point. The angles were $8°$ toe-in, from $0°$ to $12°$ toe-out in $2°$ steps, and finally $16°$ toe-out. For each β, tests were conducted at 3 different turbine diameter Reynolds numbers, 3, 4 and $5 \cdot 10^5$, yielding a total of 27 experimental cases.

The rotor shaft was horizontally supported by two air bearings that ensured an extremely low friction when rotating. Hence, power losses due to dry friction were negligible in these experiments. A rotating torque transducer with measurement range of $5\,Nm$ and 0.20% accuracy was installed at one of the shaft ends. At the other side of the sensor, an Electromagnetic Powder Brake (EPB) with $2\,Nm$ capacity was installed. This brake allowed to set the load torque to the turbine shaft, with an accuracy of $0.005\,Nm$. Figure 3.2 shows a top view of the experimental

layout in the wind tunnel.

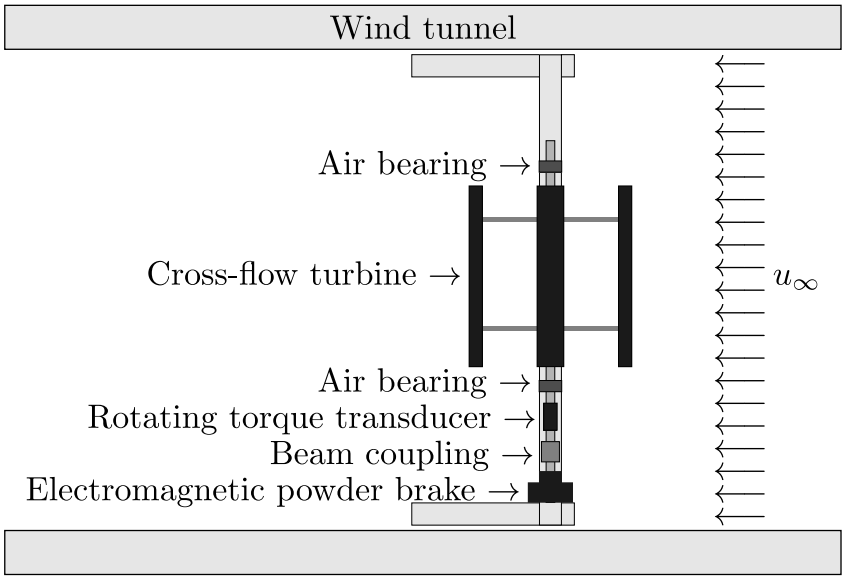

Figure 3.2: Top view of the experimental set-up in the wind tunnel.

The free stream velocity (u_∞) in the wind tunnel was measured by means of a Pitot tube. A thermocouple installed at the same point allowed the computation of a corrected air density and kinematic viscosity. The angular velocity of the rotor ω, was measured with an analogue encoder geared to the rotor shaft. In order to know the azimuthal position of the turbine, a magnetic proximity sensor installed in one of the blade struts was also used. For the experiments all signals were sampled at a rate of $2\,kHz$ during at least $60\,s$.

3.3 Results and discussion

In this section we first describe how the performance results have been obtained. A test example that appears in Figure 3.3, is used for the purpose. The dynamics of the rotor can be described by the moment equation,

$$T_B + T_R + T_A = I\alpha \tag{3.1}$$

where T_B is the blade aerodynamic torque generated by the action of the wind on the blades, T_R accounts for the resistive torque in the shaft (including elements with dry friction and the drag of the struts that support the blades), and T_A is the external applied torque or load torque, in our case applied by means of the electromagnetic powder brake. In the right hand side of the equation there is the time variation of angular momentum in the shaft, expressed as the total shaft inertia (I), assumed to be constant, times the angular acceleration $(\alpha = d\omega/dt)$. The right hand side of the equation is zero when the angular velocity of the shaft is constant, and this happens when the load torques (resistive + external brake load) balance the aerodynamic torque produced by the blades. On the other hand, if ω is not constant, the rotor is either accelerating or decelerating. It will decelerate if $T_R + T_A > T_B$, meaning that the aerodynamic torque is smaller than the existing loads acting on the rotor. The machine will only self-start accelerating if $T_R < T_B$, assuming that no brake torque is applied during this situation. In this manuscript, we

will show performance curves obtained after computing the aerodynamic blade torque (T_B), as this is in fact the net torque acting on the rotor.

The plot a) of Figure3.3 shows the sum of the brake torque applied to system plus torque resulting from the variation of the angular momentum in the shaft ($T_B + T_R = T_A + I\alpha$), as a function of the angular speed of the rotor. We use in the rest of the manuscript the terms front side and back side of the curve, in order to refer to the part of the curve at the left or right of the maximum torque, respectively. On the back side of the curve, the rotor is characterised by having a constant ω that depends on the external brake load applied, therefore Equation 3.1 reduces to $T_B + T_R = T_A$. On the front side of the curve, with ω smaller than that of the maximum torque, the rotor cannot reach constant angular velocity states and decelerates. The value of the deceleration depends on the external brake load applied T_A.

The experiments were carried out by configuring the desired free stream (or Re_D) in the wind tunnel. A DC motor geared to the rotor shaft through a $1:1$ transmission, was used to drive the turbine up to a $\omega \approx 70\, rad/s$, moment at which the DC motor was disengaged from the rotor shaft. During this process the brake was obviously not acting on the system ($T_A = 0$). The turbine then started to decelerate down to a steady condition given by a constant rotational speed. This spontaneous stabilization of the turbine was reached when the aerodynamic torque acting on the blades balanced the opposing frictional (mechanical

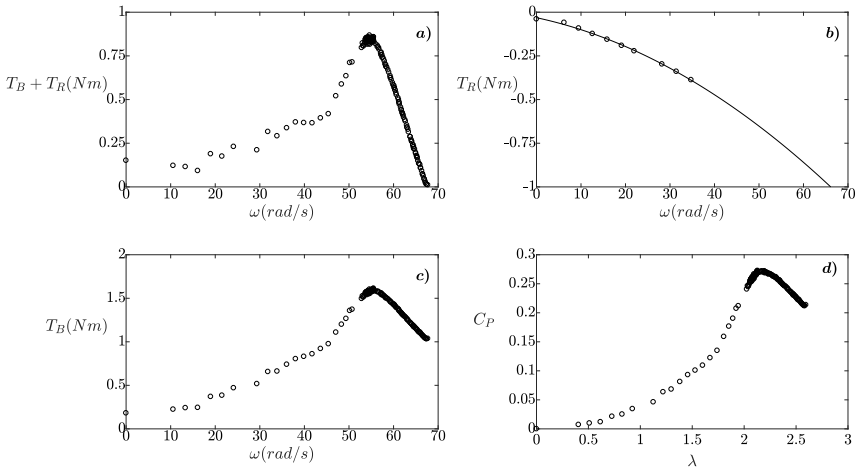

Figure 3.3: From left to right and from top to bottom: a) $T_B + T_R(\omega)$ curve, b) $T_R(\omega)$ curve, c) $T_B(\omega)$ curve, d) and performance curve.

parts rotating) plus the resistive aerodynamic torque (drag acting on the rotating struts) acting on the system.

In this state, without external load applied and spinning at the maximum ω, the time-averaged torque is zero. From that point on, the back side of the curve is obtained by applying increasing brake torque (T_A). In the experiments this was done by changing the load applied by the EPB in steps of approximately $0.005\ Nm$ and leaving time enough for the rotor to reach a new constant ω, when the blade aerodynamic torque balanced the brake and the resistive torque resultant. After each of these brake torque changes, the torque was measured during at least $60\ s$ in order to be able to compute accurate time-averaged values. Eventually, a maximum value of torque was reached that if surpassed led to the start

of the front side of the curve, with machine slowly decelerating to rest. In fact, once the maximum was surpassed, the velocity started to decrease, i.e. the aerodynamic torque was not large enough to balance the load torques (brake plus resistive). In this part the curve has a positive slope and equation 3.1 applies. Recall that $I\alpha$ value is 0 on the back side, but negative on the front side of the curve. In order to obtain the points in this part of the curve, the time series of the signals recorded were processed in time windows of $1\,s$. This is a way to obtain a moving averaged ω, giving a measure of the deceleration between two of these consecutive time windows. The same was done with the torque signal. This is a standard methodology to obtain performance curves [19].

In order to obtain the resistive torque (T_R), we carried out a series of tests at each turbine diameter Reynolds number, but this time without the blades installed in the rotor. The system was driven with the DC motor at different ω while measuring the torque on the shaft. During this type of tests, the torque load cell measured both dry friction of the components and the aerodynamic drag due to the rotating struts. By measuring at different rotational speeds, the resistive torque curve as a function of ω for each Re_D was obtained. A typical curve appears in plot b) of Figure 3.3. The values of the resistive torque are negative, with a quadratic trend imposed by the aerodynamic drag due to struts, as in the experiments presented here dry friction was minimal because the shaft was supported by air bearings. By removing this resistive torque curve from the measured torque during the experiments, depicted in Figure 3.3

a), we obtained the net blade aerodynamic torque (T_B) that is shown in plot c) of the same figure. Note that by streamlining the struts in order to reduce their aerodynamic drag, more points could have been obtained in the stable back side of the curve at higher ω. However it is not the intention of this work to produce an optimised machine in terms of design, but to understand the performance changes associated to the pitch angle variations. Plot d) of Figure 3.3 shows the final performance curve of the turbine for the example presented, i.e. the dimensionless power coefficient calculated by using T_B in Equation 1.2, as a function of the tip speed ratio (Equation 1.1).

3.3.1 The effect of Reynolds number

Having described how the results have been obtained, in this section we describe how performance curves vary with Re_D. For this purpose we have analysed one single pitch angle: $\beta = 8°$ toe-out. The left side plot in Figure 3.4 shows the performance curves for the selected blade pitch at three different Re_D. At the lowest diameter Reynolds number ($Re_D = 3 \cdot 10^3$), the CFT accelerated self-starting from rest up to a $\lambda = 1.5$, reaching a maximum power coefficient $C_P \approx 0.06$. Even if the cross-flow turbine was motor-driven to $\lambda > 1.5$, once the motor was disengaged, the turbine decelerated returning to a steady λ of 1.5. This implies that the aerodynamic torque generated by the blades could only

overcome the resistive torque at low TSRs.

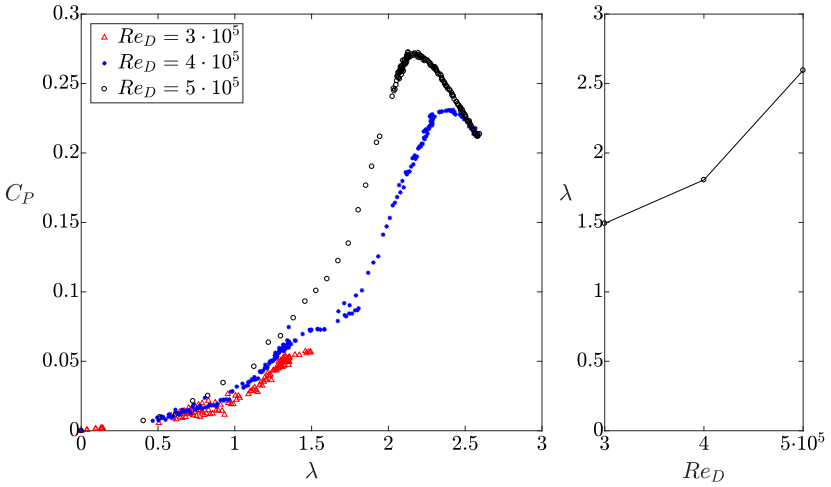

Figure 3.4: From left to right: performance curves at different diameter Reynolds numbers, and turbine neutral curve for $\beta = 8°$ toe-out.

With a Re_D of $4{\cdot}10^5$ the rotor, if not driven by the motor, accelerated from rest up to $\lambda \approx 1.7$. If the motor was used to drive the turbine shaft to tip speed ratios higher than 1.9 and disengaged afterwards, the CFT stabilized at $\lambda = 2.6$ with a maximum $C_P = 0.23$ at around $\lambda \approx 2.4$. The range of TSRs $1.7 < \lambda < 1.9$ shows the so-called *dead band* where the useful blade torque is lower than the resistive torque. In a $T_B + T_R(\omega)$ curve this region would appear with negative values. The dead could be modified or even avoided by streamlining the struts.

At the highest diameter Reynolds number $Re_D = 5 \cdot 10^5$, the dead band totally disappeared and the cross-flow turbine accelerated self-starting from rest up to a $\lambda = 2.6$, reaching a maximum power out-

put over 0.27 at a $\lambda \approx 2.1$. This self-starting behaviour implies that the blade aerodynamic torque was higher than the resistive torque at all times.

The plot on the right column of Figure 3.4 shows the neutral curve defined in Section 3.1, for the same case with blade pitch $\beta = 8°$ toe-out. The curve shows the maximum λ values that the rotor is able to reach if flow-driven without brake torque applied to it, starting from rest. The abrupt change from $Re_D = 4 \cdot 10^5$ to $5 \cdot 10^5$ can be explained because of the lack of dead band, i.e. the aerodynamic torque produced by the blades surpasses the resistive torque for all the range $0 < \lambda < 2.6$ without the need of forced-starting.

The behaviour of the cross-flow turbine with increasing Re_D described here for $\beta = 8°$ toe-out can be extrapolated to all the blade pitches tested. As the turbine diameter Reynolds number is increased from $3 \cdot 10^5$ to $5 \cdot 10^5$, the curve $T_B + T_R(\omega)$ have positive values in a larger range of TSRs. At low Re_D, T_B is higher than T_R only at low λ. At mid Re_D, there are two different ranges of tip speed ratios with positive $T_B + T_R$ values separated by a dead band. At high Re_D, this dead band disappears, allowing to obtain high power coefficients for a larger range of TSRs and displacing the maximum C_P to a lower λ. However, the Re_D that limit these three different behaviours will depend on the blade pitch angle.

3.3.2 The effect of blade pitch

In order to study the effect of blade pitch, we compare here the performance curves for nine different blade pitches in the range from $\beta = 8°$ toe-in to $16°$ toe-out, at three different constant turbine diameter Reynolds number. Figure 3.5 shows this comparison for a $Re_D = 3 \cdot 10^5$. The results demonstrate large changes in performance with very small variations of the pitch angle. The worst scenario in terms of performance took place for $\beta > 8°$ toe-out with the turbine not being able to reach TSRs larger than 0.5. The same happens at the other end of the range, for $\beta = 8°$ toe-in. With a $\beta = 0°$, the power coefficient increased considerably, although when the DC motor was disengaged at high TSRs, the turbine decelerated down to a stable $\lambda \approx 1.5$. A very similar behaviour was found for $\beta = 8°$ toe-out. Remarkably, for pitch values in the range from $2°$ to $6°$ toe-out, when the DC motor was disconnected from the rotor shaft, the CFT stabilized at a TSR near 2.5. The fact that the curve for the blade pitch of $6°$ is displaced to the right, climbing parallel to the $2°$ and $4°$ curves, after a plateau in the C_P near a TSR of 1.5, indicates the existence of a deeper dead band when the pitch is $6°$.

The data for a Reynolds number of $4 \cdot 10^5$ appears in Figure 3.6. The scenario is very similar to that reported for the smallest Re_D, with the lowest performance cases in the range from $8°$ toe-in to $0°$ and from $10°$ to $16°$ toe-out. At this slightly higher Re_D, the blade pitch of $8°$ toe-out

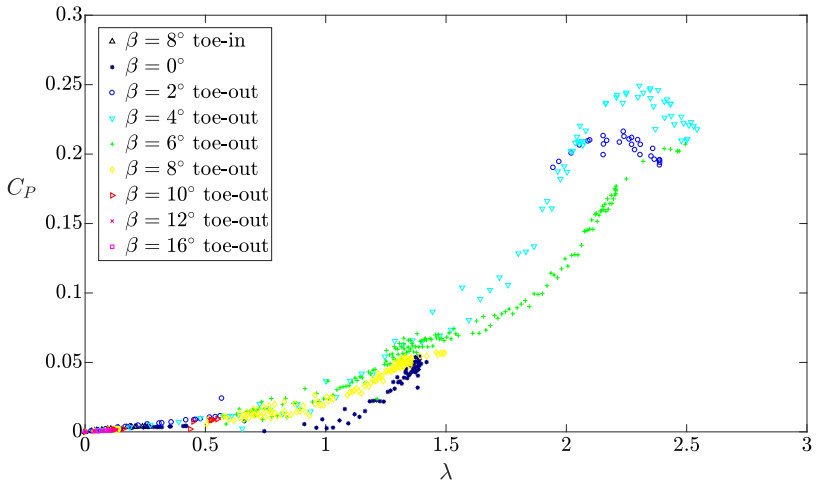

Figure 3.5: Performance curves for different pitch angles at $Re_D = 3{\cdot}10^5$.

is also producing large efficiencies. For $\beta = 4°$ and $\beta = 6°$ toe-out, the CFT already accelerated self-starting from rest up to $\lambda = 2.5$. The curve displaced to the right after a plateau around a TSR of 1.7 is now the one for blade pitch $8°$ toe-out.

Finally, the results for the highest Reynolds number investigated, $Re_D = 5 \cdot 10^5$, are presented in Figure 3.7. As in the cases of Figure 3.6, four blade pitches ($2° < \beta < 8°$ toe-out) result in curves with maxima over 0.1. $\beta = 10°$ toe-out have a very similar behaviour to the one corresponding to $\beta = 0°$. In this case the rotor accelerated self-starting from rest up to $\lambda = 2.6$ also for $\beta = 8°$ toe-out, reaching maximum values of C_P over 0.27 at $\lambda \approx 2.1$. For β in the range from $2°$ to $6°$ toe-out, the maximum power coefficient decreased, whilst in the range $8°$ to $10°$ this value was higher than at lower Re_D. This means that,

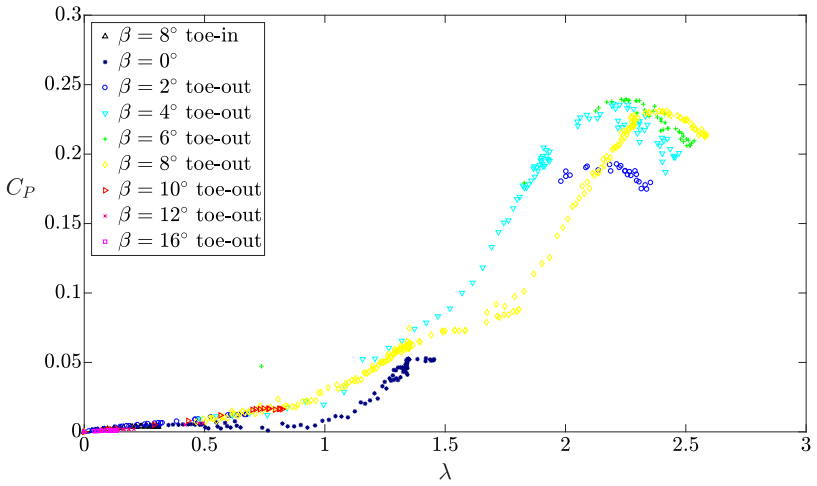

Figure 3.6: Performance curves for different pitch angles at $Re_D = 4{\cdot}10^5$.

apart from improving the performance of the cross-flow turbines, as we increased the velocity of the incoming flow, the optimal fixed blade pitch was higher.

Figure 3.8 shows the maximum power output as a function of the blade pitch angle, for the three Re_D studied. The vertical black line indicates $\beta = 0°$ for reference. For $Re_D = 3 \cdot 10^5$, there is a sharp peak with a local maximum for angles between $2°$ and $6°$, and C_P values over 0.2 and up to 0.25. As the turbine diameter Reynolds number is increased up to $Re_D = 4 \cdot 10^5$, the maxima of C_P show a wider peak with values near 0.25 for $4° < \beta < 8°$ toe-out. At the highest Re_D of $5 \cdot 10^5$, this peak is clearly moved to higher blade pitch angles with its maximum C_P over 0.27 for $\beta = 8°$ toe-out.

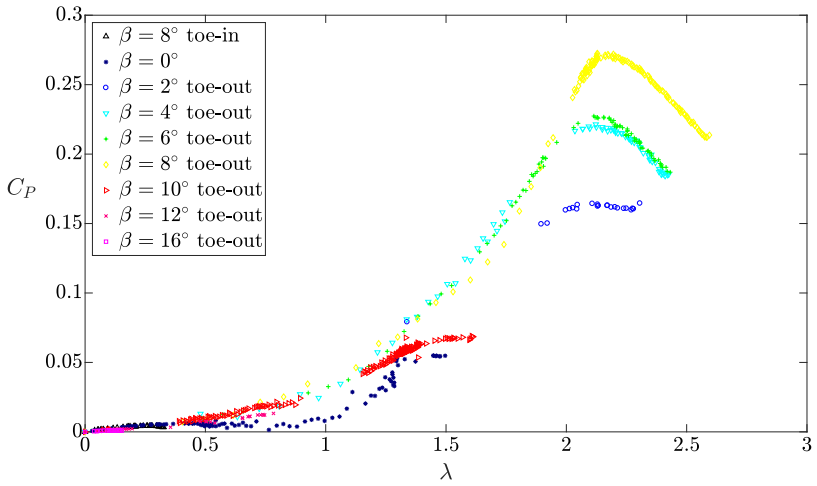

Figure 3.7: Performance curves for different pitch angles at $Re_D = 5{\cdot}10^5$.

Many authors have used a servo motor to measure the aerodynamic torque of the blades [4, 6, 11, 22, 49]. The originality of our work resides in obtaining performance curves without forcing the rotation of the turbine, what have served to deeply understand the dead band. The presence of this region where the resistive torque is superior to the blade torque at lower or higher Re_D depends clearly on the blade pitch angle imposed.

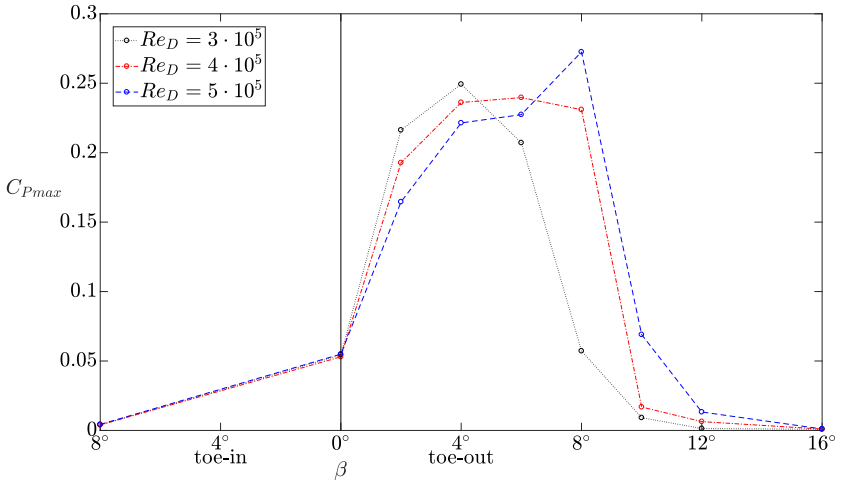

Figure 3.8: Maximum power coefficient obtained as a function of the blade pitch angle for different turbine diameter Reynolds numbers.

Chapter 4

Flow dynamics of cross-flow turbines

4.1 Introduction

To the knowledge of the author there is no reference that explain from the flow physics, the performance of the cross-flow turbines as a function of the blade pitch angles, described in Chapter 3. Although there is a large number of articles devoted to the analysis of the performance of cross-flow turbines, there are only a few that deal with the fluid dynamics of the rotor and in particular with the flow interactions

between the blades. Most of the papers that deal with the fluid dynamics of CFTs focus their attention on the near wake region downstream of the turbine or in time averaged measurements [51, 44, 41], but not inside the rotor, because of the complexity of having reliable measurements or computations in that area. To study dynamic stall, Fujisawa and Shibuya [23], and Simão Ferreira et al. [48] carried out DPIV measurements in a water and in a wind tunnel respectively, of the flow field around a rotating airfoil. In a recent numerical work by Ferrer and Willden [21], the authors defined what they called blade-wake interaction limits as the tip speed ratios that change the type of interactions in the rotor of their turbine. The regions they defined in the λ axis are dependant on how the wake of the blades that are in the upstream part of the rotor, interact with the ones in the downstream part. This dependence is established based on an axial flow speed induction factor, that they use to quantify the velocity deficit inside the rotor, and how vortices generated in the upstream part are convected and interact with the downstream ones.

The objective of this chapter is the study of the flow dynamics, and the interaction between the wakes shed by the blades of a cross-flow turbine. The performance curves obtained in Chapter 3 exhibit the three regions in the tip speed ratio axis (R_1, R_2 and R_3) commented in Section 1.3. Hence, the aim is to analyse the blade-wake interactions inside the rotor of CFTs, in order to better understand the flow physics associated to each region of the performance curves. In the experiments, the rotation of the turbine was prescribed as in Araya and Dabiri [2] and Parker

and Leftwich [41], in order to overcome the limitations imposed by the facilities available in the lab.

4.2 Experimental set-up

The CFT model was specially designed in order to generate quality DPIV measurements inside and around the rotor. Tests were carried out in the towing tank of the LIFE at URV. The facility has a cross-section that is $0.6 \times 0.6\, m^2$ and it is equipped with an AC motor controlled with a frequency variator that allows to set towing speeds. The motion of the towing carriage was measured using a precision potentiometer, so the free stream velocity u_∞ was available.

The CFT model used in the experiments consisted of a three straight bladed turbine based on a constant NACA-0015 profile with a chord $c = 28 mm$. The blades were 3D printed with polylactic acid and had a 3 mm diameter stainless steel rod in their core, in order to make them as stiff as possible, preventing displacements and vibrations of the blades during the experiments. The turbine had a diameter $D = 175\, mm$, leading to a chord to diameter ratio $c/D = 0.16$, hence the CFT model used in the experiments had the same blade profiles and turbine solidity as those used in Chapter 3. Therefore its performance curve is expected to be qualitatively similar, with the three clearly defined regions of performance

in the λ axis (R_1, R_2 and R_3).

The blades had a span $L = 150\,mm$, leading to a span to diameter ratio $L/D = 0.86$. Parker and Leftwich [41] showed how for blade aspect ratios $L/D > 0.67$, the flow field at the blade mid-span was not affected by the three-dimensional structures generated at the ends of the blade. In our experiments the three blades were cantilevered to allow complete optical access of the rotor from below. The blades were rigidly supported by two groups of connecting arms to the shaft of the turbine, made of a 6 mm diameter aluminium rod. The struts were 3D printed with PLA and were designed in order to let us change the preset fixed pitch on the blades. Taking into account the needed correction for a forward shift of the mount-point (Equation 1.6), we tested our model firstly with $\beta = 0°$. Afterwards, we use this case as a reference one, and obtained optical measurements for the toe-in pitch of $\beta = 8°$ and for the toe-out pitches of $\beta = 8°$ and $\beta = 16°$. The CFT model, made of the main shaft, the struts, and the blades ended up being very rigid and stiff, yielding no vibrations during its operation whilst providing the desired optical access to the inner part of the rotor. The rotational speed of the rotor was measured using an analogue encoder connected through a 1:1 transmission gear to the main shaft of the turbine model. In Figure 4.1 there is an schematic with the complete experimental set-up. The towing speed (u_∞) and the rotor angular speed (ω) signals were digitized by using a data acquisition system programmed to deliver a sampling rate of $1\,kHz$.

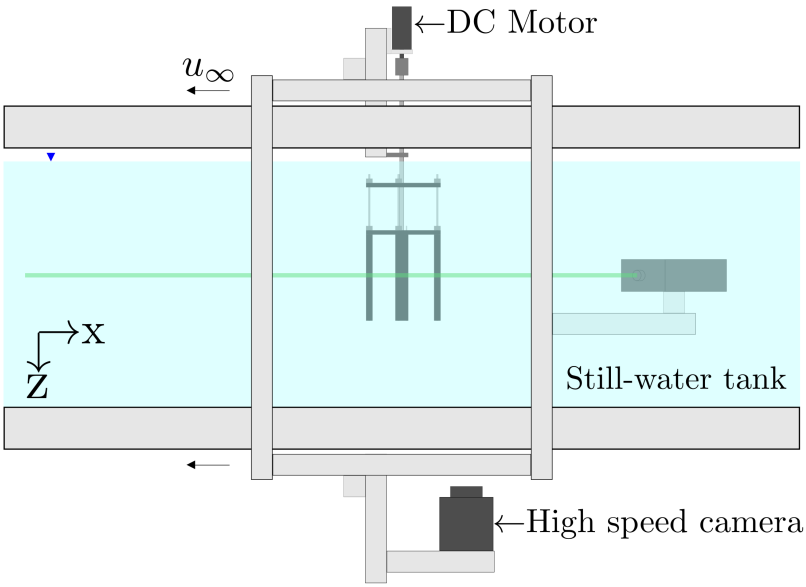

(a) Side view of the experimental set-up

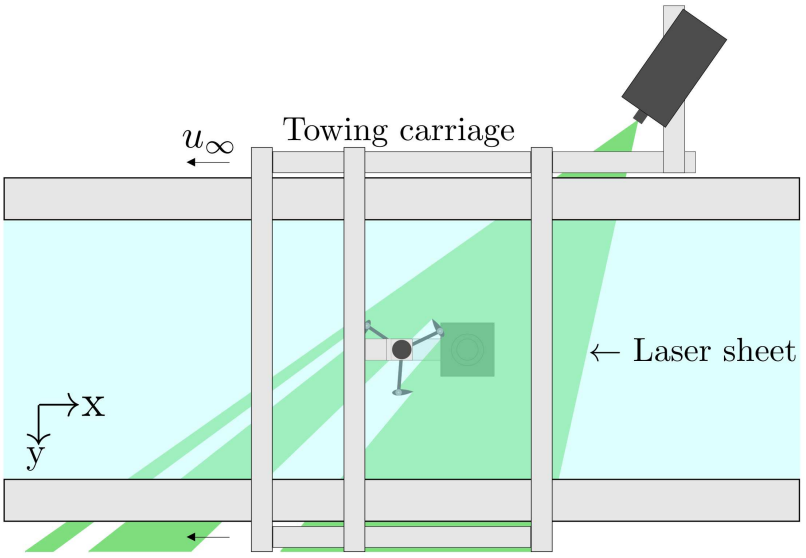

(b) Top view of the experimental set-up

Figure 4.1: Layout of the experiments in the still water towing tank.

DPIV measurements were obtained by illuminating a planar region around and inside the rotor in the towing tank, with a $5\,W$ continuous wave diode pumped solid state green laser. Polyamide seeding particles $(20\ \mu m)$ introduced in the tank scattered the laser light and images were acquired using a high speed camera based on a CCD sensor with resolution of 1280x1024 pixels. The camera was equipped with a $20\,mm$ fixed focal length lens and it was triggered to take images at $500\ fps$. After an image masking process using an in-house code, images were used to compute velocity vectors using Fast Fourier Transform (FFT) cross-correlation algorithm [55], with a $24 \times 24\,pixels\ (\approx c/3 \times c/3)$ interrogation window and a 50% overlapping. Figure 4.1 shows how the DPIV laser sheet aimed at the mid span of the blades, illuminating the inner part of the rotor and the near wake of the turbine.

The experiments were conducted by forcing the rotation of the turbine rotor using a DC motor, while being towed in the still water tank at a constant velocity of $u_\infty = 0.35\,m/s$, so all tests were carried out at a constant $Re_D = 6.1 \cdot 10^4$. With this set-up we were able to study the flow dynamics and the blade-wake interactions in our CFT model.

4.3 Results and discussion

4.3.1 The effect of tip speed ratio

Works that show the near wake evolution in straight bladed cross-flow turbines are scarce, see for example those by Tescione et al. [51], Rolin and Porté-Agel [44], and Parker and Leftwich [41]. Although there are recent numerical investigations devoted to the investigation of the flow interactions inside the rotor [21], to the knowledge of the authors there are no works purely devoted to the detailed analysis of the flow inside multi-blade rotors and its implications on the performance of CFTs. In this subsection we present the analysis of the DPIV results that allows us to describe the mechanisms of blade-wake interaction that can be associated to each performance region in the curves. The focus is given to the detailed analysis of the flow interactions in the rotor of the turbine.

In order to conduct all experiments for this subsection, β was set to $0°$. Table 4.1 shows the investigated range of λ and blade chord based Reynolds number, defined as

$$Re_c = \frac{\omega D^2 c}{2\nu} \tag{4.1}$$

The values in bold indicate those tests selected for the analysis presented in this subsection, covering the three regions in the performance curves

described previously as R_1, R_2 and R_3.

Table 4.1: Tip speed ratio (λ) and blade chord Reynolds number (Re_c) for each experiment conducted with $\beta = 0°$. In bold the experiments selected for the analysis presented in this subsection.

λ	Re_c
0.70	$6.8 \cdot 10^3$
0.85	$8.3 \cdot 10^3$
1.00	$\mathbf{9.8 \cdot 10^3}$
1.15	$1.1 \cdot 10^4$
1.30	$1.3 \cdot 10^4$
1.40	$1.4 \cdot 10^4$
1.50	$1.5 \cdot 10^4$
1.60	$1.6 \cdot 10^4$
1.70	$\mathbf{1.7 \cdot 10^4}$
1.85	$1.8 \cdot 10^4$
2.00	$2.0 \cdot 10^4$
2.15	$2.1 \cdot 10^4$
2.30	$\mathbf{2.2 \cdot 10^4}$

The smaller plots in the upper and right region of Figure 4.2, are for the dimensionless mean stream-wise velocity ($\bar{u}/u_\infty$) fields obtained for seven different tip speed ratios. The white areas in the plots are regions that become dark in the time averaged DPIV fields, because of the moving blade shadows when conducting the DPIV measurements. The black discontinuous lines in all the plots of the figure are used to indicate the size of the rotor for reference. In the main plot of the figure, velocity profiles appear for seven TSRs (with different colour), from 0.7 to 2.3, at three locations in the wake of the turbine ($0.5D$, $1.2D$ and $1.8D$). The vertical solid lines in the figure are used to emphasize the location of $\bar{u} = 0$ and $\bar{u} = u_\infty$ for each set of velocity curves. The

width of the wake is depicted with coloured dashed lines, that indicate the region in which the flow velocity is smaller than the free stream, i.e. $\bar{u} < u_\infty$. The velocity deficit region in the wake is asymmetric because of the rotation, and as the tip speed ratio is increased, the wake becomes narrower. In general velocity profiles change gradually as a function of tip speed ratio, with differences becoming more evident in the near wake and inside the rotor. At $0.5D$ there is a well-defined peak in the velocity profiles in the downstroke region for the two highest λ. The peak has practically disappeared for λ <1.5. As we move downstream in the wake, differences in the velocity profiles for the different TSRs become smaller. In general, previous studies using DPIV in the wake of cross-flow turbines [51, 44, 41] have focused their attention in the far wake of the turbine, where in fact tip speed ratio effects are difficult to observe.

The investigation of the local velocity field is of extreme interest in order to study where phenomena such as stall is prone to occur. In the experiments presented here, with blade chord based Reynolds number in the range of $6.8 \cdot 10^3 < Re_c < 2.2 \cdot 10^4$, it can be assumed that the static stall angle will remain at values very near those of Gerontakos and Lee [24], Morshed et al. [38], Rezaeiha et al. [42], and Sheldahl and Klimas [47] cited in Section 1.5 ($13° < \alpha_{ss} < 14°$).

In order to investigate the flow interactions in our turbine model, we have computed the local mean flow in the vicinity of the blades, using velocity triangles defined by the absolute flow velocity, the blade velocity

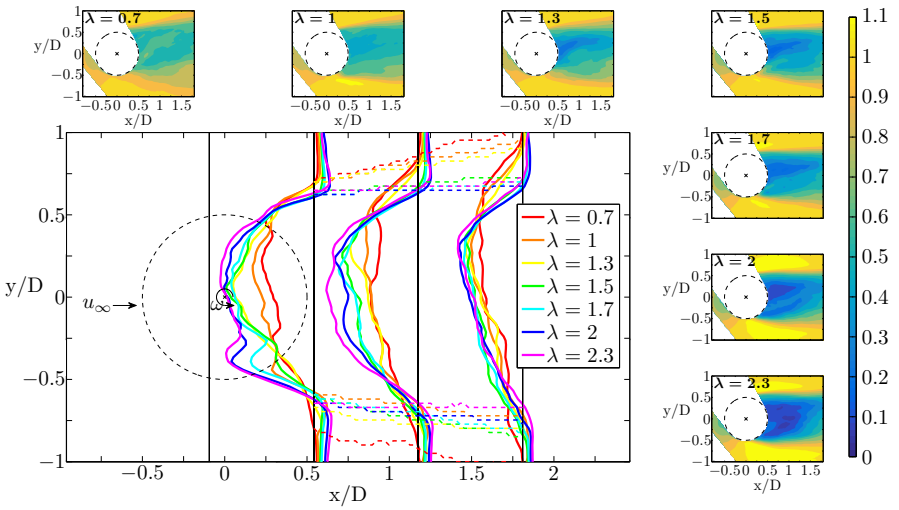

Figure 4.2: Mean dimensionless velocity fields ($\bar{u}/u_\infty$) and velocity profiles at distances 0.5D, 1.2D and 1.8D with $\beta = 0°$ for different TSRs. Dashed lines in the main plot are used to indicate the width of the wake. Vertical solid lines give the location of $\bar{u} = 0$ and $\bar{u} = u_\infty$ for each set of velocity curves.

and the flow velocity relative to the moving blade, as in Ryan et al. [45]. In general phase-locked measurements of local velocity in the vicinity of the blades are optimal for this type of analysis, but time-averaged velocity fields allow as well to obtain the local field in the vicinity of the turbine blades. In fact, it is a significant improvement when compared to the use of unperturbed bulk flow velocity to construct velocity vectors, as described by Laneville and Vittecoq [31], and Dixon et al. [17].

Velocity triangles have been computed in order to determine the effective blade angle of attack α as a function of θ. α appears in the Figure 4.3 with solid lines of different colour for each one of the three tip speed

ratios selected from Table 4.1. α has been calculated from the velocity triangles as indicated in Figure 1.2. The local velocity vector seen by a turbine blade at each azimuthal location is taken as the spatial average of a square area of 5×5 temporal averaged flow velocity vectors ($\approx c \times c$), centred at the mid-chord of the blade [45]. This way curves become soft enough without losing changes of gradient in the downstream region. The black horizontal discontinuous lines indicate the assumed static stall angle. In the figure, dashed coloured lines are for theoretical angles of attack, computed assuming the airfoil has negligible influence on the flow field as given by Equation 1.5. In the experiments reported here, with $\beta = 0°$, α only depends on λ and θ if induced velocities are neglected. The dashed-dotted lines were obtained assuming a linearly decreasing stream-wise velocity in the downstream region as in Strom et al. [49], with their maximum deficit obtained from the velocity profiles presented previously in Figure 4.2.

Differences between both versions of theoretical values and the experimental results are evident. The experimental results (solid lines) show how the angle of attack becomes positive before the blade arrive the downstream region for all tip speed ratios. The larger the tip speed ratio, the smaller θ is for α to be positive. This is because when the blades are rotating to the downstream region, there is a deflection of the flow around the turbine, so the actual local velocity has a lateral component. In the downstream region, for $\lambda = 1$ the angles of attack are larger than their theoretical values of the discontinuous lines because

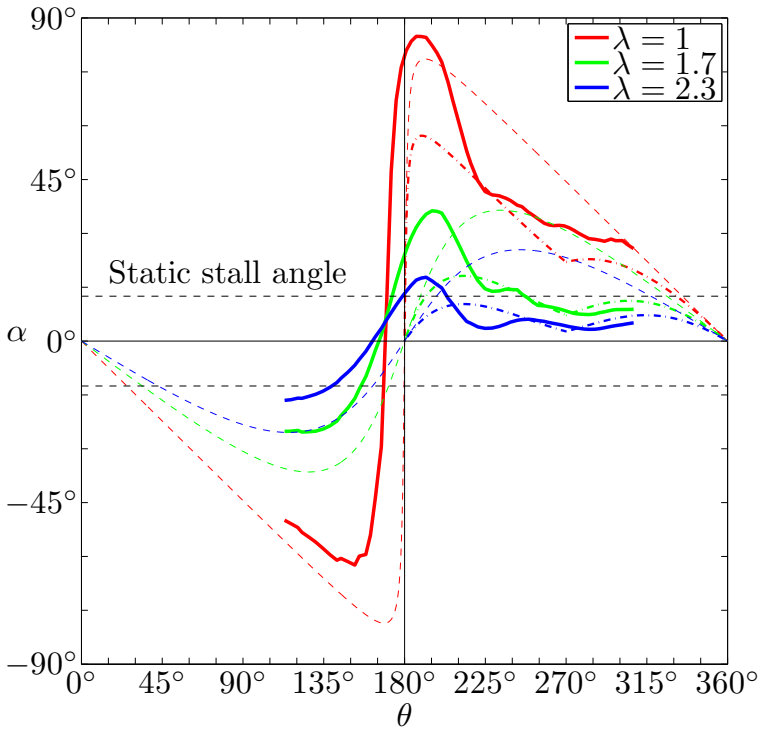

Figure 4.3: Angle of attack (α) as a function of the azimuthal location in the rotor (θ) with $\beta = 0°$ for different TSRs. Solid coloured lines are for the experimental results and the dashed and dash-dotted lines are for theoretical estimations.

the free stream velocity is dominant when computing the relative fluid velocity. On the contrary, for $\lambda = 2.3$ in this same region, experimental solid lines have smaller values than their theoretical discontinuous lines because the wake is dominated by the rotational velocity of the rotor. As the TSR increases from $\lambda = 1$ to $\lambda = 2.3$, the range of values covered by the angle of attack α is smaller and the change in its sign becomes less abrupt. It is known that once the angle of attack surpasses the static

stall limit, the increase in performance due to the increase in lift force on the airfoil, starts to be smaller than the negative effect due to the increase in the drag force. The plots in Figure 4.3 suggest exactly the same thing, with intermediate values of λ that yield moderate angles of attack high enough to have increased lift forces without excessive drag forces.

In Figure 4.2 the larger differences in the velocity profiles take place near the rotor as expected. One of the goals of this work is to investigate what is the origin of these differences and how they affect performance. In order to support the observations based on Figure 4.3, we analyse here in detail the vortex dynamics inside the rotor of the turbine. Figures 4.4–4.6 show dimensionless phase-averaged vorticity fields during one third of rotation of the turbine, for the three TSRs selected from Table 4.1. The phases for the averaging have been chosen in order to cover one third of the rotor rotation and are referred to the azimuthal angle defined in Figure 1.2. The experiment in Figure 4.4, with a $\lambda = 1$, is for a low performance case falling in the first region (R_1) described previously. The experiment in Figure 4.5, with a $\lambda = 1.7$, is for a case with performance near the peak in the $C_P(\lambda)$ curve, in the second region (R_2) described. Finally the run in Figure 4.6 with a $\lambda = 2.3$, shows an experiment in region R_3, in which the performance is again low because the tip speed ratio is way too high. These three experiments have been selected in between all the runs conducted, after a detailed analysis, because they represent the typical flow dynamics inside each major performance region.

For the case with $\lambda = 1$ in region R_1 (Figure 4.4), each blade tends to behave as an isolated bluff body, with the rotor flow dominated by the free stream velocity. When the blade is moving from $\theta = 90°$ to $180°$, α grows to more than $-60°$ (see Figure 4.3) and two vortices are formed. A leading-edge vortex, L1 in the plots, is formed and travels inside the rotor to the downstream region. A Trailing-Edge Vortex (TEV), T1 in the plots, is also shed from the blade when it passes through $\theta = 135°$. The * symbol that appears in some of the vortices in the plots, indicates that the vortex was shed by previous blades. As the blade continues its motion, circulation is generated around it, creating a second pair of vortices (T2 and L2) that is fully formed at $\theta = 195°$. At this position in the rotor, there is a strong interaction between the first pair of vortices (T1, L1) and the last one (T2, L2). In fact L1 and L2 form a counter-rotating pair at the leading edge of the blade. Something similar takes place at the trailing edge of the blade, T1 forms another counter-rotating pair with T2. As a consequence of this interaction and this large region of unsteady flow, the local wake of the blade is heavily deflected radially. In fact, it was seen how for the case with $\lambda = 1$, the effective angle of attack resulted in $\alpha \approx 90°$ at θ slightly larger than $180°$, indicating this local radial flow and suggesting a large drag force on the foil. This could be inferred from the observation presented in Figure 4.3, but the physical explanation is given here, thanks to the analysis of the vortex dynamics in the rotor. In the upstroke region, vorticity emanating from the upstream region dissipates quickly, hence as soon as the blades reach a $\theta = 30°$ the wake interactions become weaker.

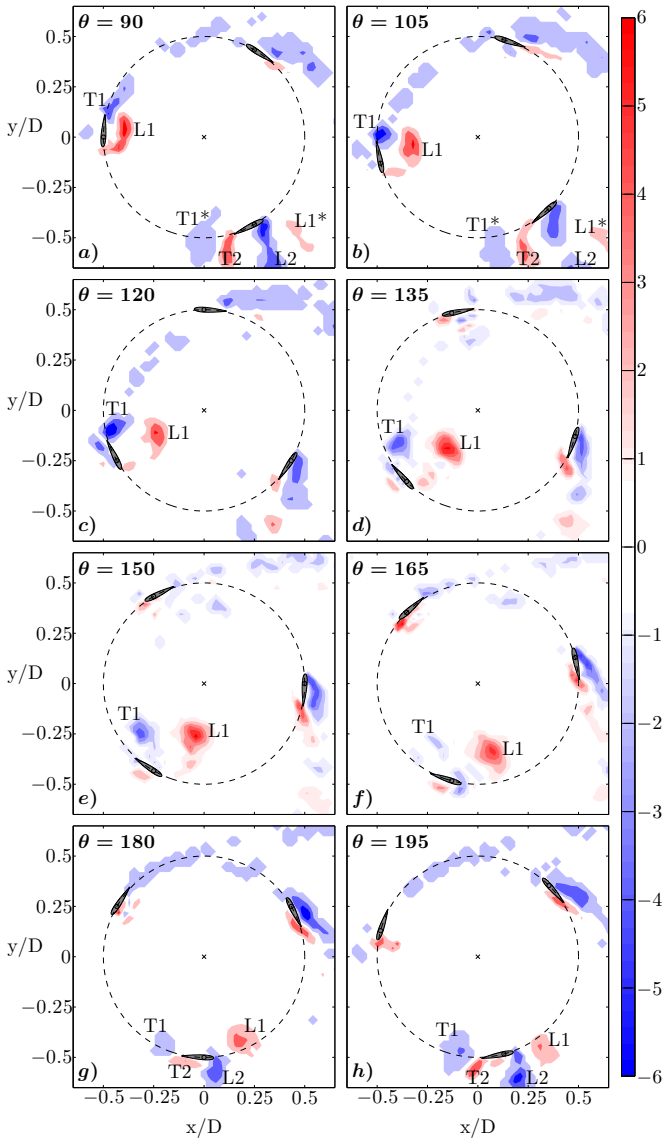

Figure 4.4: Phase-averaged dimensionless vorticity maps ($\Omega \cdot c/u_\infty$) at eight azimuthal positions (θ) at $\lambda = 1$ for $\beta = 0°$. Red indicates counter-clockwise vorticity. In all the plots flow is left to right and the turbine is rotating counter-clockwise.

When $\lambda = 1.7$ (region R_2) as in Figure 4.5, the performance of this type of turbine is known to be higher than at $\lambda = 1$ (region R_1), and the flow interactions taking place inside the rotor are remarkably different. The formation of the LEV L1 is delayed, and its detachment from the blade takes place roughly when the blade reaches a θ of more than $135°$, instead of $105°$ as with $\lambda = 1$. At the trailing edge of the blade, a series of shear layer vortices are formed that quickly dissipate and travel in the upstroke region of the rotor. The blade moves to larger θ faster than the vortices are convected inside the rotor, and by the time it is at $\theta = 195°$, the vortex that the same blade shed at $135°$ does not affect the formation of L2 and T2 as strongly as in the case with $\lambda = 1$. In fact the blade sees the LEV shed by the blade ahead, which at this location has lost most of its circulation. With $\lambda = 1.7$, the local wake of the blade when moving through the downstroke region is very different to that seen in Figure 4.4, with $\lambda = 1$. The relative flow in the blade promotes a larger tangential component if compared with the case with $\lambda = 1$, where it was seen that the main characteristic was a strong radial component in the wake. This is somehow also indicated by the results presented in Figure 4.3, in which the maximum α achieved was smaller (approximately $30°$) for a larger θ (around $200°$). This flow topology associated with a larger tangential component of the local flow around the blades, suggests smaller drag forces and therefore larger torques in the shaft in region R_2 if compared to those in region R_1.

In region R_3, with $\lambda = 2.3$ as in Figure 4.6, the wake is dominated

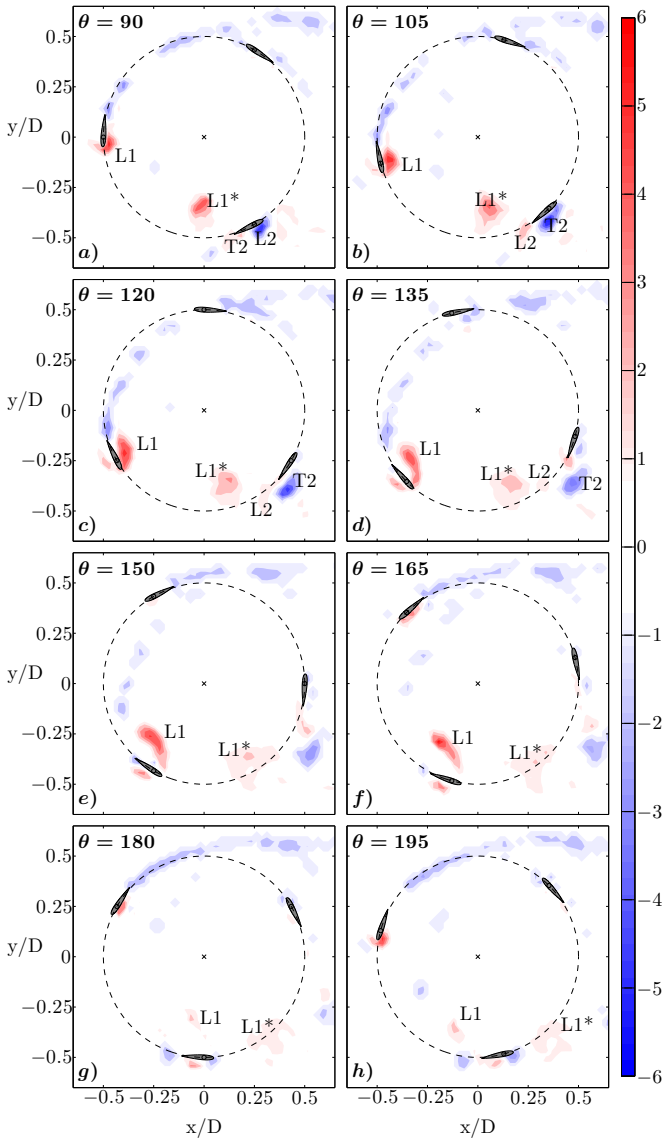

Figure 4.5: Phase-averaged dimensionless vorticity maps ($\Omega \cdot c/u_\infty$) at eight azimuthal positions (θ) at $\lambda = 1.7$ for $\beta = 0°$. Red indicates counter-clockwise vorticity. In all the plots flow is left to right and the turbine is rotating counter-clockwise.

by the rotational velocity of the rotor. The LEV remains attached to the surface of the blade translating towards its trailing edge, suggesting a smaller lift force on the foil. Its shedding is delayed to a θ near $180°$, where it remains until the blade behind cuts through it, generating a flow that resembles the shear layer flow in the upstroke region. This blocked flow in the downstroke part is the reason why there is a well-defined peak in the velocity profile of Figure 4.2. It is also obvious from Figure 4.3 that the rate of change of α with θ is a lot smaller and the maximum value achieved stays under $20°$.

The DPIV results give a detailed view of the blade flow interaction phenomena inside the rotor, and allow to explain the large variations in the performance of this type of turbines. The analysis of the local velocities around the blades and the vortex dynamics in the rotor is crucial in order to provide a physical explanation for the performance changes in a cross-flow turbine, operating at different tip speed ratios. The three experiments analysed in this subsection, clearly show three very distinct types of blade-wake interactions inside the rotor of the turbine, that can be related to three very distinct performances as a function of tip speed ratio. Although it is not the intention of this work to establish the tip speed ratios at which the changes in performance associated to the changes in the vortex dynamics take place, from the analysis of the rest of the cases available (Table 4.1) it is easy to observe the progressive changes in the vortex dynamics, from the situation presented in Figure 4.4 to the one in Figure 4.6. We provide in Figure 4.7 an schematic with

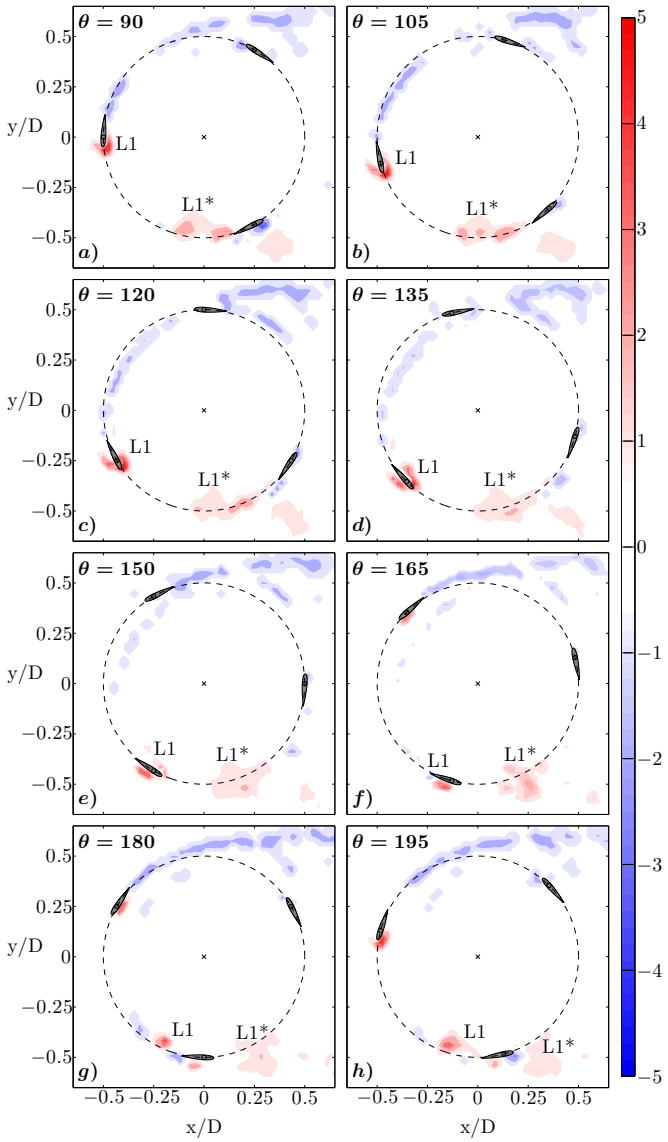

Figure 4.6: Phase-averaged dimensionless vorticity maps ($\Omega \cdot c/u_\infty$) at eight azimuthal positions (θ) at $\lambda = 2.3$ for $\beta = 0°$. Red indicates counter-clockwise vorticity. In all the plots flow is left to right and the turbine is rotating counter-clockwise.

the different blade-wake interactions that have been clearly identified and related to the three regions in the performance curve of a three straight bladed cross-flow turbine. In all three images one of the blades is at $\theta = 105°$. The way the vortex pair $L1^* - T1^*$ is convected inside the rotor, largely modifies the vortex dynamics around the blade when it reaches the downstream part of the rotor, producing a large change in the local flow, and hence in the performance of the CFT.

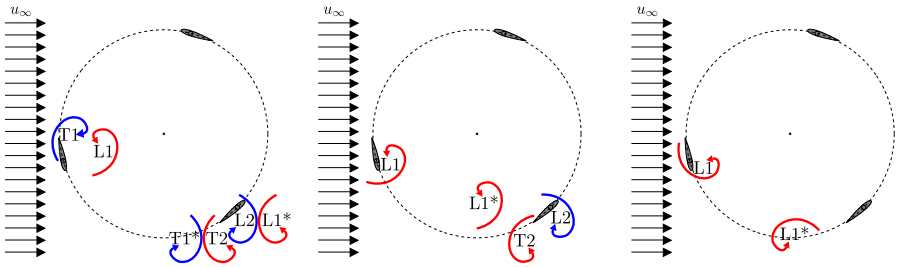

(a) $\lambda = 1$ (region R_1) (b) $\lambda = 1.7$ (region R_2) (c) $\lambda = 2.3$ (region R_3)

Figure 4.7: Schematic representation of the vortex dynamics in a three straight bladed CFT, as a function of the tip speed ratio for $\beta = 0°$. In all three images one of the blades is at $\theta = 105°$.

The general framework that allows the physical understanding of the changes in the rotor flow with tip speed ratio, has been presented here. However, the vortex dynamics, and therefore the performance in this type of turbines is very dependant on blade pitch. The analysis of the effect of variations in the pitch angle is presented in Subsection 4.3.2.

4.3.2 The effect of blade pitch

To the knowledge of the author there are no works entirely devoted to the study of the effects of the pitch angle on the blade-wake interactions of a straight-bladed CFT using DPIV measurements inside the rotor. In this subsection we present detailed flow physics analysis for different β at several TSRs greater than 1.5. The results for $\beta = 0°$ of Subsection 4.3.1 are used here for reference.

In these tests, a total of 13 different rotational speeds for each blade pitch, resulted in the 52 combinations showed in Table 4.2. The tip speed ratios that appear in bold in the table, indicate those tests selected for the analysis presented in this subsection.

Table 4.2: Combinations of blade pitches and tip speed ratios of the 52 tests conducted. In bold the TSRs selected for the analysis presented in this subsection.

$\boldsymbol{\beta}$	$8°$ toe-in	$0°$	$8°$ toe-out	$16°$								
$\boldsymbol{\lambda}$	0.70	0.85	1.00	1.15	1.30	1.40	1.50	1.60	$\mathbf{1.70}$	1.85	2.00	2.15	$\mathbf{2.30}$

Figures 4.8–4.9 show dimensionless mean stream-wise velocities ($\bar{u}/u_\infty$) for the two TSRs selected from Table 4.2. In each of the two figures, the smaller plots in the right column are for the dimensionless mean stream-wise velocity fields obtained for each preset fixed pitch, namely $\beta = 8°$ toe-in, $\beta = 0°$, $\beta = 8°$ and $\beta = 16°$ toe-out. Because the moving blade blocked the laser light when conducting the DPIV measurements, there

are regions that were not instantaneously illuminated, so they appear as white regions in the plots. The size of the rotor is indicated with black dashed lines in all the plots. In the main plot of the figures, velocity profiles appear for the four β with different colour, at three locations in the wake of the turbine ($0.5D$, $1.2D$ and $1.8D$). At each location, $\bar{u} = 0$ and $\bar{u} = u_\infty$ are indicated using vertical black lines for reference. The coloured dashed lines give an estimate of the width of the wake, i.e. the region in which the flow velocity $\bar{u}$ is smaller than the free stream one u_∞.

Figure 4.8 presents the experiments conducted with $\lambda = 1.7$. With $\beta = 0°$, at a distance of $0.5D$, the wake is asymmetric because of the rotation, with its largest velocity deficit in the upstroke region except from one well-defined peak in the downstroke area. As we change the pitch angle to $\beta = 8°$ toe-in, the downstroke peak tends to decrease moving the maximum velocity deficit towards the upstroke region. On the other hand, with $\beta = 8°$ toe-out, the deficit peak in the downstroke region increases up to its maximum value. Beyond this toe-out position, a corridor of higher velocities appears at the centre of the rotor. This effect of having enhanced velocities crossing the rotor becomes important with increasing β. Differences between the velocity profiles caused by β, become less evident as we move downstream in the wake.

An experiment conducted with $\lambda = 2.3$ is presented in Figure 4.9. The mean flow and the velocity profiles for $\beta = 8°$ toe-in, practically do

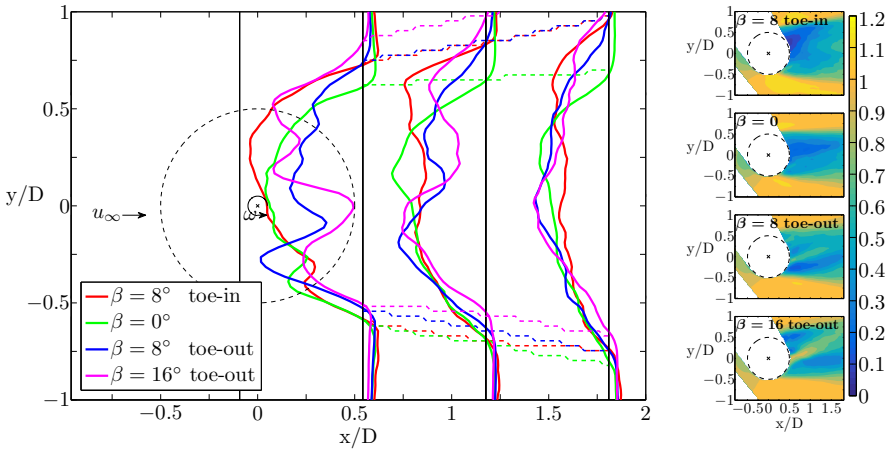

Figure 4.8: Mean dimensionless velocity fields ($\bar{u}/u_\infty$) and velocity profiles at distances 0.5D, 1.2D and 1.8D at $\lambda = 1.7$ for different β. Dashed lines in the main plot are used to indicate the width of the wake.

not change with λ. With $\beta = 0°$ the wake seems to be more symmetric, there is a larger velocity deficit and the flow outside the wake moves faster than at $\lambda = 1.7$. As β is changed to $8°$ toe-out, the deficit peak in the downstroke region reaches negative values at the distance $0.5D$, indicating a flow against the current in the near wake. Besides, the wake is narrower and the inner flow corridor crossing the rotor, that was incipient at $\lambda = 1.7$, has practically vanished at $\lambda = 2.3$. As β is increased to $16°$ toe-out, the corridor of higher velocities in the downstroke area becomes larger, and a second parallel one appears in the upstroke region. It is remarkable how for both TSRs, in the far wake of the CFT (where most of the previous studies have focused their attention [41, 44, 51]) the rich dynamics taking place in the near wake have practically disappeared. This reveals the importance of analysing the flow inside the rotor to understand the performance of this type of

machines.

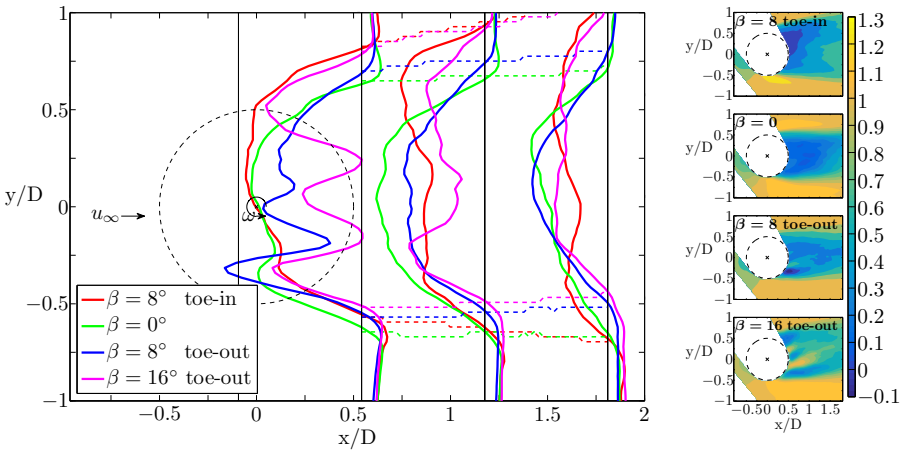

Figure 4.9: Mean dimensionless velocity fields ($\bar{u}/u_\infty$) and velocity profiles at distances 0.5D, 1.2D and 1.8D at $\lambda = 2.3$ for different β. Dashed lines in the main plot are used to indicate the width of the wake.

In order to determine the effective angle of attack seen by a turbine blade at each azimuthal location, we have used as in Subsection 4.3.1, the time-averaged fields to compute the spatial average of 5×5 local velocity vectors ($\approx c \times c$) centred at the mid-chord of the blade. This spatial average smoothens $\alpha(\theta)$ curves without losing data in the downstream region.

Figures 4.10–4.11 show $\alpha(\theta)$ for the two TSRs selected from Table 4.2, with solid lines in which the colour indicates the different blade pitches tested. Because of the moving blades and the laser illumination when conducting the DPIV measurements, there are regions inside the rotor in which time-averaged data are not available, corresponding to areas without values in the plots. The black horizontal dashed lines

represent the assumed static stall angle in Subsection 4.3.1. Dashed coloured lines are for the theoretical angles of attack, computed using equation

$$\alpha = -\tan^{-1}\left[\frac{\sin(\theta+\beta)}{\lambda+\cos(\theta+\beta)}\right] \tag{4.2}$$

where β is positive in the toe-in rotation. Note that induced velocities are neglected in the equation. The dash-dotted lines result from taking the velocity deficit in the downstream region into account, assuming a linearly decreasing stream-wise velocity in this region, with their maximum deficit obtained from the velocity profiles presented previously in Figures 4.8–4.9. The first difference between both versions of the theoretical values and the experimental results is that in these last ones, the angle of attack becomes positive before the blade arrives the downstream region for all blade pitches. This difference is due to a deflection of the flow around the turbine when blades are rotating to the downstream region, hence the actual local velocity has a lateral component.

Figure 4.10 shows the angle of attack as a function of the azimuthal location in the case of $\lambda = 1.7$ for the four different pitches. The angle of attack curves have the same slope for all β at θ near $180°$, and as the blade pitch is changed towards toe-out positions α becomes positive at higher azimuthal angles. Nevertheless, the difference between these θ (at which the angle of attack becomes positive) for two consecutive pitch angles is less than $8°$ as indicated by the theoretical curves. Previous an-

alytical expressions (Equation 1.7) do not consider that as β increases in the toe-out direction, the drop of α in the downstream region is delayed. The expression proposed in this work (Equation 4.2) does account for this fact. Data suggest that for $\beta = 8°$ toe-in, the low angles of attack in the downstream region cause a small lift force component that leads to a decrease in the overall performance. For $\beta = 16°$ toe-out, the high α in this region may result in excessive drag forces, being detrimental to the power output too.

Figure 4.11 presents $\alpha(\theta)$ curves for the four different β at $\lambda = 2.3$. For all of them, in the downstream region experimental solid lines have smaller values of α than their theoretical discontinuous lines because the wake is dominated by the rotational velocity of the rotor. As the TSR is increased the amplitude of the angles of attack decreases, and the fluctuations of α in the downstream region become larger, reaching its highest values at $\theta > 225°$ for $\beta = 16°$ toe-out. These fluctuations differ from theoretical curves, as these last ones even considering the velocity deficit in the downstream region (dash-dotted lines), they do it assuming a linearly decreasing stream-wise velocity, which is obviously not strictly happening (Figures 4.8–4.9).

In order to investigate what is the origin of differences in the velocity profiles and to support the observations based on Figures 4.10–4.11, we have analysed in detail how blade pitch alters the vortex dynamics inside the rotor at a given TSR. The general behaviour of the blade-

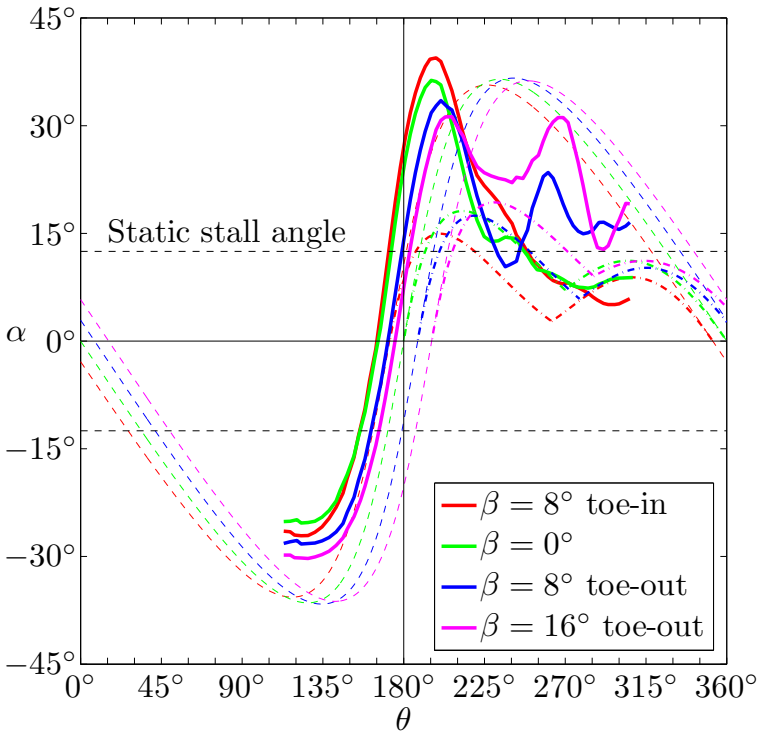

Figure 4.10: Angle of attack (α) as a function of the azimuthal location in the rotor (θ) at $\lambda = 1.7$ for different β. Solid coloured lines are for the experimental results and the dashed and dash-dotted lines are for theoretical estimations proposed in this work.

wake interaction phenomena inside the rotor (being dominated by the rotational motion as the TSR is increased) is similar whatever the blade pitch is. Moreover at any given TSR, the large difference between the vortex dynamics inside the rotor when presetting different fixed blade pitches is that the shedding of the vortex pair formed in the upstream region is delayed as β is changed from $\beta = 8°$ toe-in to $\beta = 16°$ toe-out. Hence, we focus the attention here at a single tip speed ratio. Figures

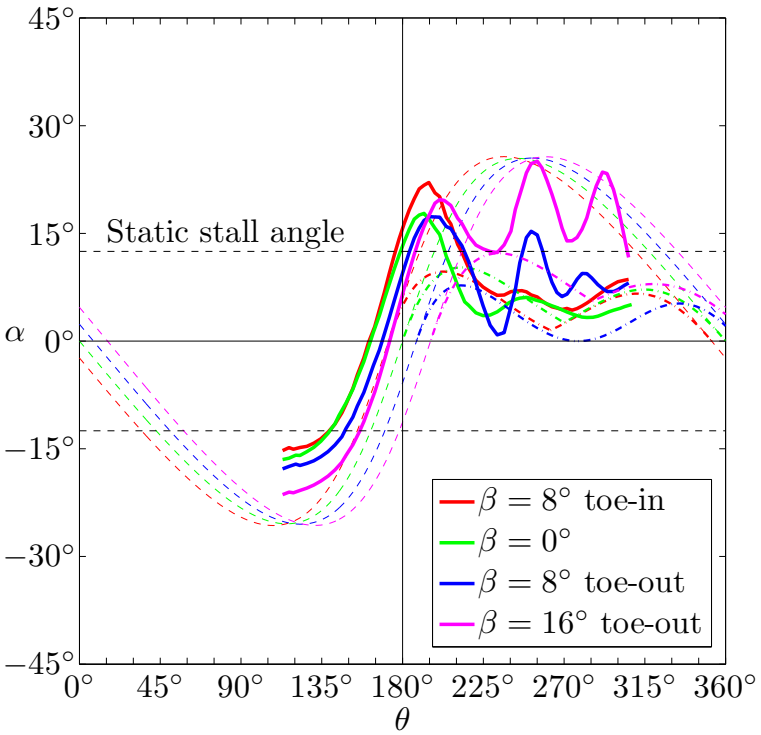

Figure 4.11: Angle of attack (α) as a function of the azimuthal location in the rotor (θ) at $\lambda = 2.3$ for different β. Solid coloured lines are for the experimental results and the dashed and dash-dotted lines are for theoretical estimations proposed in this work.

4.12–4.14 show phase-averaged dimensionless vorticity fields during one third of rotation of the turbine at $\lambda = 1.7$ for blade pitches $\beta \neq 0°$.

For the case of $\beta = 8°$ toe-in, when the blade is moving from $\theta = 90°$ to $180°$, α reaches a value of more than $-25°$ (Figure 4.10). In Figure 4.12, a LEV, L1 in the plots, is shed just before the blade passes through $\theta = 120°$, and travels inside the rotor towards the downstream region.

A series of shear layer vortices are also formed at the trailing edge of the blade and travel to the upstroke part of the rotor, dissipating quickly. As the blade continues its motion to larger azimuthal angles, circulation is generated around it and a second pair of vortices is created: L2 and the trailing-edge vortex T2. Because the blade rotates faster than the vortices are convected inside the rotor, L1 does not strongly affect the formation of L2 and T2. In fact, at this point the blade sees the LEV shed by the blade ahead, which has lost most of its circulation. The * symbol is referred to the vortex shed by previous blades. The red dash-dotted line represents the trajectory of L1 for $\beta = 8°$ toe-in. For reference, the black dash-dotted line is used to show the trajectory of the same LEV when $\beta = 0°$. It can be clearly seen how the detachment of L1 is advanced as blade pitch is moved towards toe-in positions. This fact supports the proposed Equation 4.2 as a good analytical expression for what happens in the rotor. With $\beta = 8°$ toe-in the L1 follows a trajectory further away from the blade.

Figure 4.13 shows phase-averaged dimensionless vorticity fields for $\beta = 8°$ toe-out. In this case, as we were expecting, the detachment of the LEV L1 is delayed until the blade almost reaches the azimuthal angle $\theta = 150°$. Therefore, its trajectory inside the rotor to the downstream region, represented in red dash-dotted line, is closer to the blade than the one for $\beta = 0°$, indicated by the black dash-dotted line. This way the LEV L1, once is shed from the blade, travels closer to the blade exerting larger forces on it, suggesting an improvement of the performance of

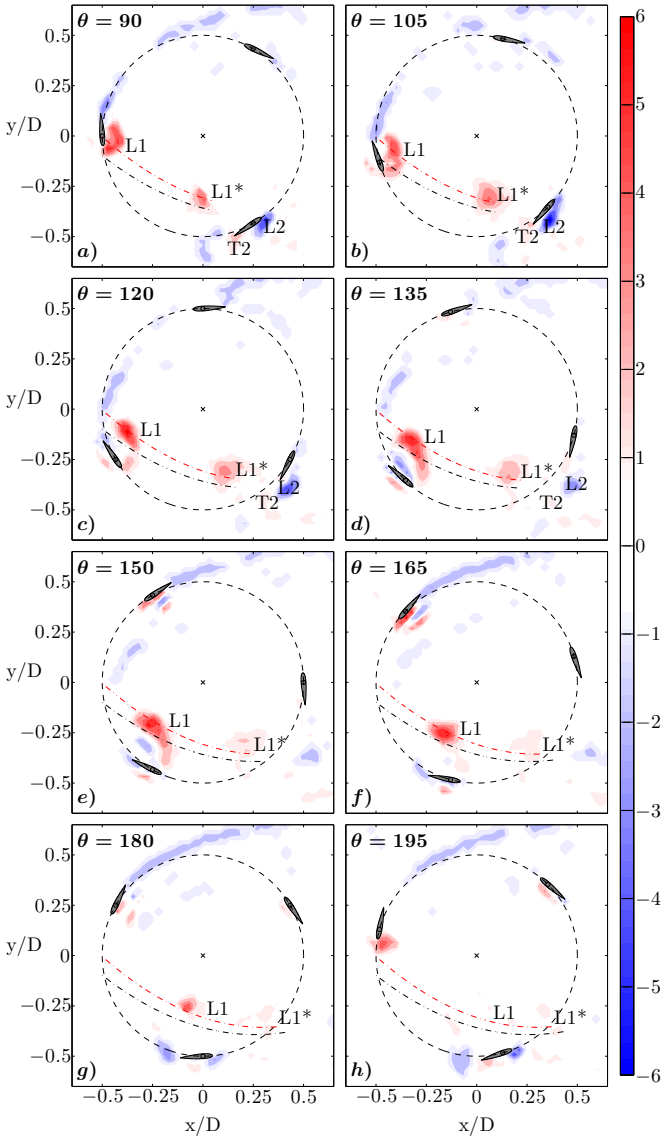

Figure 4.12: Phase-averaged dimensionless vorticity maps ($\Omega \cdot c/u_\infty$) at eight azimuthal positions (θ) at $\lambda = 1.7$ for $\beta = 8°$ toe-in. Red indicates counter-clockwise vorticity. In all the plots flow is left to right and the turbine is rotating counter-clockwise. Dash-dotted lines represent the trajectory of L1 for $\beta = 0°$ (black) and for $\beta = 8°$ toe-in (red).

the CFT [31, 23]. This trajectory is the reason why there is a well-defined peak in the downstroke region of its velocity profile in Figure 4.8. Besides, before finishing its path in the downstroke region, where it mostly contributes to the power output of the turbine, other two pair of vortices are shed: L2-T2 y L3-T3. The TEV T3 can be inferred from Figure 4.10 with another positive ramp of the angle of attack in the downstream part of the turbine, being responsible for maintaining high lift forces until the downstroke region is finished.

The phase-averaged dimensionless vorticity maps for $\beta = 16°$ toe-out are presented in Figure 4.14. Here, the trajectory of the LEV L1 does not appear because it remains attached to the blade translating towards its trailing edge. Its shedding takes place when the blade passes through $\theta = 180°$. The flow structures suggest a larger drag force on the foil, and hence a lower performance of the CFT. In this case the other two pairs of vortices are largely delayed and TEV T3 is not shed until the upstroke region. This is the reason why there is also a well-defined velocity deficit peak in the upstroke region at the velocity profile as shown in Figure 4.8. The maximum lift is expected to be substantially smaller when the counter-clockwise vortex passes below the blade [1].

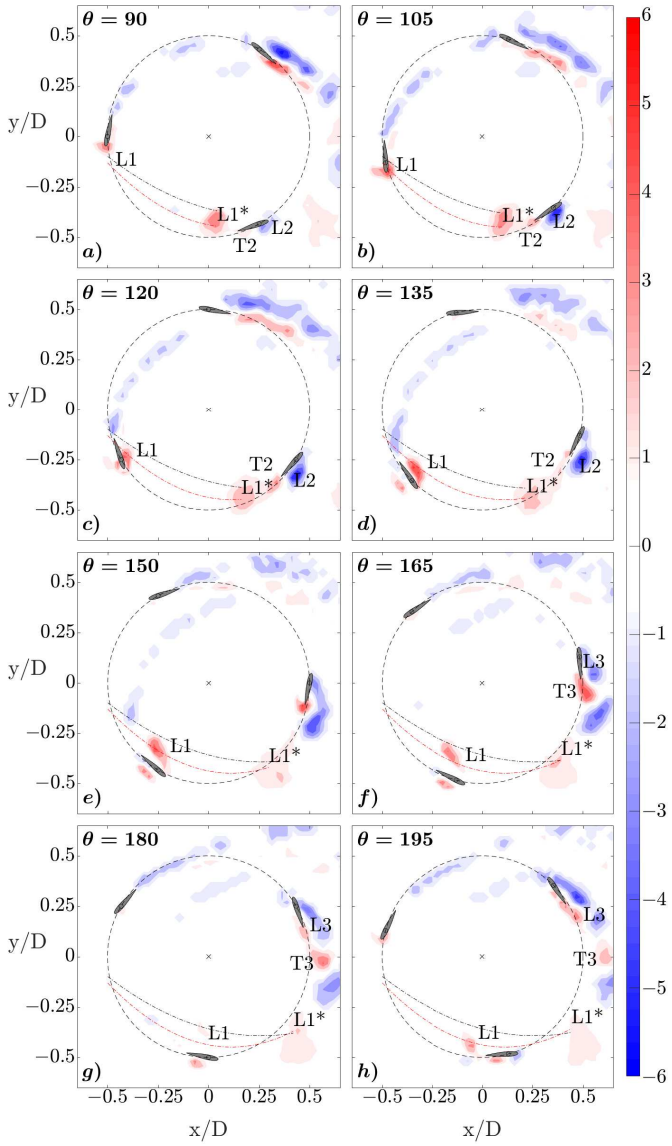

Figure 4.13: Phase-averaged dimensionless vorticity maps ($\Omega \cdot c/u_\infty$) at eight azimuthal positions (θ) at $\lambda = 1.7$ for $\beta = 8°$ toe-out. Red indicates counter-clockwise vorticity. In all the plots flow is left to right and the turbine is rotating counter-clockwise. Dash-dotted lines represent the trajectory of L1 for $\beta = 0°$ (black) and for $\beta = 8°$ toe-out (red).

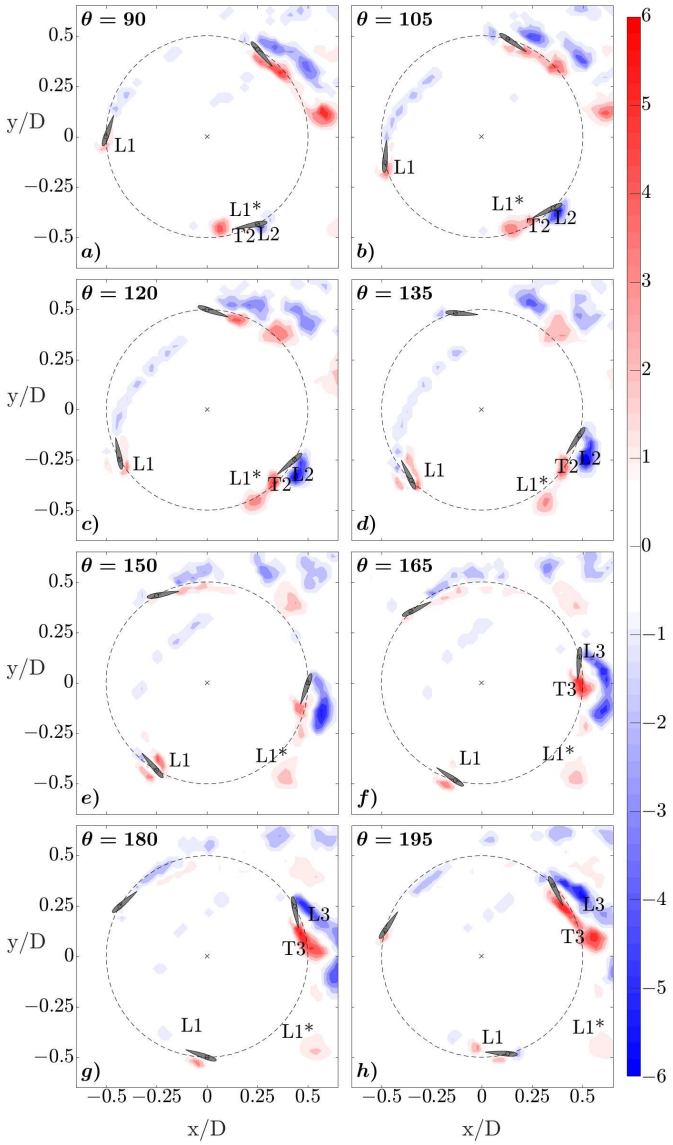

Figure 4.14: Phase-averaged dimensionless vorticity maps ($\Omega \cdot c/u_\infty$) at eight azimuthal positions (θ) at $\lambda = 1.7$ for $\beta = 16°$ toe-out. Red indicates counter-clockwise vorticity. In all the plots flow is left to right and the turbine is rotating counter-clockwise.

Chapter 5

Conclusions

Firstly, detailed experiments have been conducted in a wind tunnel with a three straight bladed cross-flow turbine based on symmetric profiles in order to study the combined effects of turbine diameter Reynolds number and blade pitch. Experiments have been carried at three Re_D in the range from $3 \cdot 10^5$ to $5 \cdot 10^5$, and for each one, the effect of the pitch angle has been studied with nine different values between 8° toe-in and 16° toe-out.

The turbine model demonstrated a high performance when blade pitch was configured between $\beta = 4^\circ$ and $\beta = 8^\circ$ toe-out. It is remarkable however, that the efficiency is highly dependant on small variations of the pitch angle. This angle is crucial as it imposes the torque produced

by the blades and the ability of the rotor to overcome resistive loads.

The transitional region in which the blade torque surpasses the resistive torque, is clearly defined on the $\beta = 8°$ toe-out case. At low Reynolds number $Re_D = 3 \cdot 10^5$ the useful blade torque is only superior at low tip speed ratios $\lambda < 1.7$. Nevertheless, as we increase the velocity of the incoming flow, another stable back side of the performance curve appears at high tip speed ratios $\lambda > 1.9$. The dead band where the resistive torque due to the aerodynamic drag on the struts of the model is superior, gets to disappear when the u_∞ was large enough. At high diameter Reynolds number $Re_D = 5 \cdot 10^5$ there is no lack of self-starting any more.

For every pitch angle, once the stable back side of the $C_P(\lambda)$ curve has appeared at large tip speed ratios, the higher the Re_D, the lower the optimal tip speed ratio at which the maximum power coefficient takes place. In the cases of $\beta = 4°$ and $\beta = 6°$ toe-out, the cross-flow turbine has the ability of self-starting already at $Re_D = 4 \cdot 10^5$. Besides, the optimal pitch angle with which we obtain the maximum dimensionless power output of the turbine changes from $\beta = 4°$ to $\beta = 8°$ toe-out as the diameter Reynolds number is increased. Between all cases, the maximum C_P over 0.27 is obtained with this last fixed blade pitch at $Re_D = 5 \cdot 10^5$ and $\lambda = 2.1$.

Secondly, experiments carried out in a water tank with another tur-

bine model of smaller scale but the same characteristics of solidity and blade profiles, have allowed us to explain the performance differences in this type of turbines as a function of the operational tip speed ratio and the blade pitch. With a fixed pitch angle of $\beta = 0°$, we have shown how the analysis of the vortex dynamics inside the rotor is necessary in order to explain the physical mechanisms that lead to changes in the performance as λ is increased.

At low tip speed ratios, the wake is dominated by the free stream and there is a strong interaction between the vorticity generated in the upstream region of the turbine and the downstream one. The wake of the blade in the downstroke part of the rotor promotes a local flow dominated by a radial component. For intermediate tip speed ratios, in the region in which the power output is the largest, the flow interactions inside the rotor result in local velocity vectors with larger tangential components. If the tip speed ratio is too large, the wake of the turbine becomes narrower and although the downstream part of the turbine is affected by a largely unsteady incoming flow, the local wake of each blade is dominated by the rotational motion and therefore by a small lift component.

Finally, planar velocimetry results show the local velocities and the vortex dynamics inside the rotor with different preset pitch angles in the range from 8° toe-in to 16° toe-out. The detailed analysis of the blade-wake interaction phenomena gives a physical explanation for the large variations in the performance of this type of turbines that are known to

take place with small variations in the pitch angle.

We have proposed a new equation for the angle of attack as a function of the azimuthal position after detailed measurements of the local velocities around the blades. We show how the vortex dynamics inside the rotor are largely altered by the pitch angle of the blade, which is key to understand the performance of CFTs. We give a fluid mechanical explanation based on the analysis of the blade-wake interactions, for the highest performance curve obtained with a pitch angle of 8° toe-out.

In future works, we would like to study the behaviour of flexible blades in a straight bladed cross-flow turbine. The idea is to add a flexible tip to the blades that would introduce a passive variable pitch, in order to understand how the $\beta(\theta)$, and hence the performance curve vary as a function of its stiffness.

Bibliography

[1] J. Alaminos-Quesada and R. Fernandez-Feria. Effect of the angle of attack on the transient lift during the interaction of a vortex with a flat plate. potential theory and experimental results. *Journal of Fluids and Structures*, 74:130–141, 2017. doi: 10.1016/j.jfluidstructs.2017.07.013.

[2] D. B. Araya and J. O. Dabiri. A comparison of wake measurements in motor-driven and flow-driven turbine experiments. *Experiments in Fluids*, 56(7):150, 2015. doi: 10.1007/s00348-015-2022-7.

[3] M. M. Aslam Bhutta, N. Hayat, A. U. Farooq, Z. Ali, S. R. Jamil, and Z. Hussain. Vertical axis wind turbine - a review of various configurations and design techniques. *Renewable and Sustainable Energy Reviews*, 16(4):1926–1939, 2012. doi: 10.1016/j.rser.2011.12.004.

[4] P. Bachant and M. Wosnik. Performance and near-wake measurements for a vertical axis turbine at moderate reynolds num-

ber. In *Proceedings of the ASME 2013 Fluids Engineering Summer Meeting*, volume 1 B, Incline Village (NV, USA), 2013. doi: 10.1115/FEDSM2013-16575.

[5] P. Bachant and M. Wosnik. Reynolds number dependence of cross-flow turbine performance and near-wake characteristics. In *Proceedings of the 2nd Marine Energy Technology Symposium*, Seattle (WA, USA), 2014.

[6] P. Bachant and M. Wosnik. Effects of reynolds number on the energy conversion and near-wake dynamics of a high solidity vertical-axis cross-flow turbine. *Energies*, 9(2):1–18, 2016. doi: 10.3390/en9020073.

[7] J. R. Baker. Features to aid or enable self starting of fixed pitch low solidity vertical axis wind turbines. *Journal of Wind Engineering and Industrial Aerodynamics*, 15(1–3):369–380, 1983. doi: 10.1016/0167-6105(83)90206-4.

[8] D. Barsky, A. Posa, M. Rahromostaqim, M. C. Leftwich, and E. Balaras. Experimental and computational wake characterization of a vertical axis wind turbine. In *Proceedings of the 32nd AIAA Applied Aerodynamics Conference*, Atlanta (GA, USA), 2014. doi: 10.2514/6.20143141.

[9] A. Betz. Das maximum der theoretisch möglichen ausnützung des windes durch windmotoren. *Zeitschrift für das gesamte Turbinenwesen*, 26:307–309, 1920.

[10] M. Boudreau and G. Dumas. Comparison of the wake recovery of the axial-flow and cross-flow turbine concepts. *Journal of Wind Engineering and Industrial Aerodynamics*, 165:137–152, 2017. doi: 10.1016/j.jweia.2017.03.010.

[11] R. Bravo, S. Tullis, and S. Ziada. Performance testing of a small vertical-axis wind turbine. In *Proceedings of the 21st Canadian Congress of Applied Mechanics*, Toronto (Ontario, Canada), 2007.

[12] S. Brusca, R. Lanzafame, and M. Messina. Design of a vertical-axis wind turbine: how the aspect ratio affects the turbine's performance. *International Journal of Energy and Environmental Engineering*, 5(4):333–340, 2014. doi: 10.1007/s40095-014-0129-x.

[13] T. C. Corke and F. O. Thomas. Dynamic stall in pitching airfoils: Aerodynamic damping and compressibility effects. *Annual Review of Fluid Mechanics*, 47:479–505, 2015. doi: 10.1146/annurev-fluid-010814-013632.

[14] J. O. Dabiri. Potential order-of-magnitude enhancement of wind farm power density via counter-rotating vertical-axis wind turbine arrays. *Journal of Renewable and Sustainable Energy*, 3(4), 2011. doi: 10.1063/1.3608170.

[15] L. A. Danao, O. Eboibi, and R. Howell. An experimental investigation into the influence of unsteady wind on the performance of a vertical axis wind turbine. *Applied Energy*, 107:403–411, 2013. doi: 10.1016/j.apenergy.2013.02.012.

[16] G. J. M. Darrieus. Turbine having its rotating shaft transverse to the flow of the current. US Patent 1835018, 1931.

[17] K. Dixon, C. Simão Ferreira, C. Hofemann, G. van Bussel, and G. van Kuik. A 3d unsteady panel method for vertical axis wind turbines. In *Proceedings of the European Wind Energy Conference and Exhibition 2008*, volume 6, pages 2981–2990, Brussels (Belgium), 2008.

[18] I. Dobrev and F. Massouh. Cfd and piv investigation of unsteady flow through savonius wind turbine. volume 6, pages 711–720, 2011. doi: 10.1016/j.egypro.2011.05.081.

[19] J. M. Edwards, L. Angelo Danao, and R. J. Howell. Novel experimental power curve determination and computational methods for the performance analysis of vertical axis wind turbines. *Journal of Solar Energy Engineering, Transactions of the ASME*, 134(3), 2012. doi: 10.1115/1.4006196.

[20] M. El-Samanoudy, A. A. E. Ghorab, and S. Z. Youssef. Effect of some design parameters on the performance of a giromill vertical axis wind turbine. *Ain Shams Engineering Journal*, 1(1):85–95, 2010. doi: 10.1016/j.asej.2010.09.012.

[21] E. Ferrer and R. H. J. Willden. Blade-wake interactions in cross-flow turbines. *International Journal of Marine Energy*, 11:71–83, 2015. doi: 10.1016/j.ijome.2015.06.001.

[22] A. J. Fiedler and S. Tullis. Blade offset and pitch effects on a high solidity vertical axis wind turbine. *Wind Engineering*, 33(3): 237–246, 2009. doi: 10.1260/030952409789140955.

[23] N. Fujisawa and S. Shibuya. Observations of dynamic stall on darrieus wind turbine blades. *Journal of Wind Engineering and Industrial Aerodynamics*, 89(2):201–214, 2001. doi: 10.1016/S0167-6105(00)00062-3.

[24] P. Gerontakos and T. Lee. PIV study of flow around unsteady airfoil with dynamic trailing-edge flap deflection. *Experiments in Fluids*, 45(6):955–972, 2008. doi: 10.1007/s00348-008-0514-4.

[25] D. N. Gorelov. Analogy between a flapping wing and a wind turbine with a vertical axis of revolution. *Journal of Applied Mechanics and Technical Physics*, 50(2):297–299, 2009. doi: 10.1007/s10808-009-0040-z.

[26] R. Howell, N. Qin, J. Edwards, and N. Durrani. Wind tunnel and numerical study of a small vertical axis wind turbine. *Renewable Energy*, 35(2):412–422, 2010. doi: 10.1016/j.renene.2009.07.025.

[27] M. Islam, D. S.-K. Ting, and A. Fartaj. Aerodynamic models for darrieus-type straight-bladed vertical axis wind turbines. *Renewable and Sustainable Energy Reviews*, 12(4):1087–1109, 2008. doi: 10.1016/j.rser.2006.10.023.

[28] B. Kirke. *Vertical axis wind turbines with particular emphasis on*

self-acting variable pitch Darrieus type turbines. PhD thesis, Griffith University (Australia), US and UK, 2011, 1998.

[29] B. K. Kirke and L. Lazauskas. Limitations of fixed pitch darrieus hydrokinetic turbines and the challenge of variable pitch. *Renewable Energy*, 36(3):893–897, 2011. doi: 10.1016/j.renene.2010.08.027.

[30] J. Kjellin, F. Bülow, S. Eriksson, P. Deglaire, M. Leijon, and H. Bernhoff. Power coefficient measurement on a 12 kw straight bladed vertical axis wind turbine. *Renewable Energy*, 36(11):3050–3053, 2011. doi: 10.1016/j.renene.2011.03.031.

[31] A. Laneville and P. Vittecoq. Dynamic stall: The case of the vertical axis wind turbine. *Journal of Solar Energy Engineering - Transactions of the ASME*, 108(2):140–145, 1986.

[32] Q. Li, T. Maeda, Y. Kamada, J. Murata, T. Kawabata, and K. Furukawa. Analysis of aerodynamic load on straight-bladed vertical axis wind turbine. *Journal of Thermal Science*, 23(4):315–324, 2014. doi: 10.1007/s11630-014-0712-8.

[33] Q. Li, T. Maeda, Y. Kamada, J. Murata, M. Yamamoto, T. Ogasawara, K. Shimizu, and K. T. Study on power performance for straight-bladed vertical axis wind turbine by field and wind tunnel test. *Renewable Energy*, 90:291–300, 2016. doi: 10.1016/j.renene.2016.01.002.

[34] S. Li and Y. Li. Numerical study on the performance effect of solidity on the straight-bladed vertical axis wind turbine. In *Proceedings*

of the 1st Asia-Pacific Power and Energy Engineering Conference, Wuhan (China), 2010. doi: 10.1109/APPEEC.2010.5449269.

[35] P. B. S. Lissaman. Wind turbine airfoils and rotor wakes. In *Wind Turbine Technology: Fundamental Concepts in Wind Turbine Engineering*, chapter 6, pages 283—-323. ASME Press, New York (NY, USA), 2009. doi: 10.1115/1.802601.ch6.

[36] D. W. MacPhee and A. Beyene. Fluid-structure interaction analysis of a morphing vertical axis wind turbine. *Journal of Fluids and Structures*, 60:143–159, 2016. doi: 10.1016/j.jfluidstructs.2015.10.010.

[37] W. J. McCroskey. The phenomenon of dynamic stall. Technical Report NASA Technical Memorandum B1264, USAAVRADCOM TR 81-A-6, Ames Research Center, Moffett Field (CA, US), 1981.

[38] M. Morshed, S. B. Sayeed, S. A. A. Mamun, and G. M. J. Alam. Investigation of drag analysis of four different profiles tested at subsonic wind tunnel. *Journal of Modern Science and Technology*, 2 (2):113–126, 2014.

[39] L. C. Pagnini, M. Burlando, and M. P. Repetto. Experimental power curve of small-size wind turbines in turbulent urban environment. *Applied Energy*, 154:112–121, 2015. doi: 10.1016/j.apenergy.2015.04.117.

[40] I. Paraschivoiu. *Wind turbine designs – with emphasis on Darrieus*

concept. Polytechnic International Press, Montreal (QC, Canada), 2009.

[41] C. M. Parker and M. C. Leftwich. The effect of tip speed ratio on a vertical axis wind turbine at high reynolds numbers. *Experiments in Fluids*, 57(5):74, 2016. doi: 10.1007/s00348-016-2155-3.

[42] A. Rezaeiha, I. Kalkman, and B. Blocken. Effect of pitch angle on power performance and aerodynamics of a vertical axis wind turbine. *Applied Energy*, 197:132–150, 2017. doi: 10.1016/j.apenergy.2017.03.128.

[43] S.-C. Roh and S.-H. Kang. Effects of a blade profile, the reynolds number, and the solidity on the performance of a straight bladed vertical axis wind turbine. *Journal of Mechanical Science and Technology*, 27(11):3299–3307, 2013. doi: 10.1007/s12206-013-0852-x.

[44] V. Rolin and F. Porté-Agel. Wind-tunnel study of the wake behind a vertical axis wind turbine in a boundary layer flow using stereoscopic particle image velocimetry. *Journal of Physics: Conference Series*, 625(1):012012, 2015. doi: 10.1088/1742-6596/625/1/012012.

[45] K. J. Ryan, F. Coletti, C. J. Elkins, J. O. Dabiri, and J. K. Eaton. Three-dimensional flow field around and downstream of a subscale model rotating vertical axis wind turbine. *Experiments in Fluids*, 57 (3):38, 2016. doi: 10.1007/s00348-016-2122-z.

[46] S. J. Savonius. The s-rotor and its application. *Journal of Mechanical Engineering*, 53(5):333–338, 1931.

[47] R. E. Sheldahl and P. C. Klimas. Aerodynamic characteristics of seven symmetrical airfoil sections through 180-degree angle of attack for use in aerodynamic analysis of vertical axis wind turbine. Technical Report Sandia Energy Report SAND80-2114, Sandia National Laboratories, Alburquerque (NM, US), 1981.

[48] C. Simão Ferreira, G. van Kuik, G. van Bussel, and F. Scarano. Visualization by PIV of dynamic stall on a vertical axis wind turbine. *Experiments in Fluids*, 46(1):97–108, 2009. doi: 10.1007/s00348-008-0543-z.

[49] B. Strom, B. S., and P. B. Consequences of preset pitch angle on cross-flow turbine hydrodynamics. In *Proceedings of the 11th European Wave and Tidal Energy Conference*, Nantes (France), 2015.

[50] M. Takao, H. Kuma, T. Maeda, Y. Kamada, M. Oki, and A. Minoda. A straight-bladed vertical axis wind turbine with a directed guide vane row - effect of guide vane geometry on the performance. *Journal of Thermal Science*, 18(1):54–57, 2009. doi: 10.1007/s11630-009-0054-0.

[51] G. Tescione, D. Ragni, C. He, C. J. Simão Ferreira, and G. J. W. van Bussel. Near wake flow analysis of a vertical axis wind turbine

by stereoscopic particle image velocimetry. *Renewable Energy*, 70: 47–61, 2014. doi: 10.1016/j.renene.2014.02.042.

[52] L. J. Vermeer, J. N. Sørensen, and A. Crespo. Wind turbine wake aerodynamics. *Progress in Aerospace Sciences*, 39(6–7):467–510, 2003. doi: 10.1016/S0376-0421(03)00078-2.

[53] K. Wang, K. Sun, Q.-H. Sheng, L. Zhang, and S.-Q. Wang. The effects of yawing motion with different frequencies on the hydrodynamic performance of floating vertical-axis tidal current turbines. *Applied Ocean Research*, 59:224–235, 2016. doi: 10.1016/j.apor.2016.06.007.

[54] R. W. Whittlesey, S. Liska, and J. O. Dabiri. Fish schooling as a basis for vertical axis wind turbine farm design. *Bioinspiration and Biomimetics*, 5(3), 2010. doi: 10.1088/1748-3182/5/3/035005.

[55] C. E. Willert and M. Gharib. Digital particle image velocimetry. *Experiments in Fluids*, 10(4):181–193, 1991. doi: 10.1007/BF00190388.

List of Figures

List of Tables

List of Abbreviations

AC: Alternating Current.

AFT: Axial-Flow Turbine.

BLWT: Boundary Layer Wind Tunnel.

CCD: Charge-Coupled Device.

CFD: Computational Fluid Dynamics.

CFT: Cross-Flow Turbine.

DC: Direct Current.

DPIV: Digital Particle Image Velocimetry.

EPB: Electromagnetic Powder Break.

FFT: Fast Fourier Transform.

HAWT: Horizontal Axis Wind Turbine.

LEV: Leading-Edge Vortex.

LIFE: Laboratory for Fluid-Structure Interaction.

NACA: National Advisory Committee for Aeronautics.

PLA: PolyLactic Acid.

TEV: Trailing-Edge Vortex.

TSR: Tip Speed Ratio.

URV: Universitat Rovira i Virgili.

VAWT: Vertical Axis Wind Turbine.

List of Publications

M. Somoano, F. J. Huera-Huarte. Flow dynamics inside the rotor of a three straight bladed cross-flow turbine. *Applied Ocean Research*, 69:138–147, 2017. doi: 10.1016/j.apor.2017.10.007.

M. Somoano, F. J. Huera-Huarte. The effect of reynolds number and blade pitch on the performance of a three straight bladed cross-flow turbine. *Submitted*, 2018.

M. Somoano, F. J. Huera-Huarte. The effect of blade pitch on the flow dynamics inside the rotor of a three straight bladed cross-flow turbine. *Submitted*, 2018.

Conferences

M. Somoano, F. J. Huera-Huarte. Poster: Planar velocimetry in the wake of a cross-flow turbine. *68th Annual Meeting of the APS Division of Fluid Dynamics*, Boston (MA, USA), 2015.

M. Somoano, F. J. Huera-Huarte. Two-dimensional flow field downstream of a cross-flow turbine. *Workshop on Fluid Mechanics 2016*, Cádiz (España), 2016.

M. Somoano, F. J. Huera-Huarte. The effect of blade pitch in the rotor hydrodynamics of a cross-flow turbine. *69th Annual Meeting of the APS Division of Fluid Dynamics*, Portland (OR, USA), 2016.

R. B. Barber, C. S. Hill, P. F. Babuska, M. Somoano, R. Wiebe, A. Aliseda, M. R. Motley. Adaptive pitch marine hydrokinetic turbine blades: experimental loading, performance and wake imaging. *5th Annual Marine Energy Technology Symposium*, Washington (DC, USA), 2017.

M. Somoano, F. J. Huera-Huarte. The effect of blade pitch and reynolds number on the performance of cross-flow turbines. *ASME 2018 37th International Conference on Ocean, Offshore and Arctic Engineering*, Madrid (España), 2018.

UNIVERSITAT ROVIRA I VIRGILI
PERFORMANCE AND FLOW DYNAMICS IN CROSS-FLOW TURBINES
Miguel Somoano Rodríguez

UNIVERSITAT ROVIRA I VIRGILI
PERFORMANCE AND FLOW DYNAMICS IN CROSS-FLOW TURBINES
Miguel Somoano Rodríguez